



**HAL**  
open science

# Joint analysis of GOCE gravity gradients data of gravitational potential and of gravity with seismological and geodynamic observations to infer mantle properties

Marianne Greff-Lefftz, Laurent Métivier, Isabelle Panet, Lambert Caron,  
Gwendoline Pajot-Métivier, Johannes Bouman

## ► To cite this version:

Marianne Greff-Lefftz, Laurent Métivier, Isabelle Panet, Lambert Caron, Gwendoline Pajot-Métivier, et al.. Joint analysis of GOCE gravity gradients data of gravitational potential and of gravity with seismological and geodynamic observations to infer mantle properties. *Geophysical Journal International*, 2016, 205 (1), pp.257-283. 10.1093/gji/ggw002 . hal-02356507

**HAL Id: hal-02356507**

**<https://hal.science/hal-02356507>**

Submitted on 18 Aug 2020

**HAL** is a multi-disciplinary open access archive for the deposit and dissemination of scientific research documents, whether they are published or not. The documents may come from teaching and research institutions in France or abroad, or from public or private research centers.

L'archive ouverte pluridisciplinaire **HAL**, est destinée au dépôt et à la diffusion de documents scientifiques de niveau recherche, publiés ou non, émanant des établissements d'enseignement et de recherche français ou étrangers, des laboratoires publics ou privés.

# Joint analysis of GOCE gravity gradients data of gravitational potential and of gravity with seismological and geodynamic observations to infer mantle properties

Marianne Greff-Lefftz,<sup>1</sup> Laurent Métivier,<sup>2</sup> Isabelle Panet,<sup>2</sup> Lambert Caron,<sup>1</sup> Gwendoline Pajot-Métivier<sup>2</sup> and Johannes Bouman<sup>3</sup>

<sup>1</sup>*Institut de Physique du Globe de Paris–Sorbonne Paris Cité, Université Paris Diderot, UMR CNRS 7154, Paris, France. E-mail: greff@ipgp.fr*

<sup>2</sup>*Institut National de l'Information Géographique et Forestière, LAREG, Université Paris Diderot, Paris, France*

<sup>3</sup>*Deutsches Geodätisches Forschungsinstitut der Technischen Universität München (DGFI-TUM), Munich, Germany*

Accepted 2016 January 5. Received 2016 January 4; in original form 2015 July 10

## SUMMARY

Joint analysis of the seismic velocities and geoid, gravity and gravity gradients are used to constrain the viscosity profile within the mantle as well as the lateral density variations. Recent ESA's Gravity field and steady-state Ocean Circulation Explorer measurements of the second-order derivatives of the Earth's gravity potential give new possibilities to determine these mantle properties. Using a simple mantle model and seismic tomography results, we investigate how the gravitational potential, the three components of the gravity vector and the gravity gradients can bring information on the radial viscosity profile and on the mantle mass anomalies. We start with lateral density variations in the Earth's mantle based either on slab history or deduced from seismic tomography. The main uncertainties are: for the latter case, the relationship between seismic velocity and density—the so-called density/velocity scaling factor—and for the former case, the variation with depth of the density contrast between the cold slabs and the surrounding mantle. We perform a Monte Carlo search for the viscosity and the density/velocity scaling factor profiles within the mantle, which allows to fit the observed geoid, gravity and gradients of gravity. We compute the posterior probability distribution of the unknown parameters, and find that the gravity gradients improve the estimate of the scaling factor within the upper mantle, because of their sensitivity to the masses within the upper mantle, whereas the geoid and the gravity better constrain the scaling factor in the lower mantle. In the upper mantle, it is less than 0.02 in the upper part and about 0.08–0.14 in the lower part, and it is significantly larger for depths greater than 1200 km (about 0.32–0.34). In any case, the density/velocity scaling factor between 670 and 1150 km depth is not well constrained. We show that the viscosity of the upper part of the mantle is strongly correlated with the viscosity of the lower part of the mantle and that the viscosity profile is characterized by a decrease in the lower part of the upper mantle (about  $10^{20}$ – $2 \times 10^{20}$  Pa s) and by an increase (about  $10^{23}$ – $2 \times 10^{23}$  Pa s) at the top of the lower mantle (between 670 and 1150 km). The viscosity of the mantle below 1150 km depth is well estimated in our Monte Carlo search and is about  $10^{22}$ – $4 \times 10^{22}$  Pa s.

**Key words:** Satellite geodesy; Gravity anomalies and Earth structure; Mantle processes; Dynamics; gravity and tectonics.

## 1 INTRODUCTION

From 2009 to 2013, the ESA's Gravity field and steady-state Ocean Circulation Explorer (GOCE) satellite measured the spatial derivatives of the Earth's gravity field in three different directions. These measurements have led to a better understanding of the physics of the upper mantle, with new insights into the geodynamics of the lithosphere, into mantle composition and rheology, uplift and

subduction processes (Ebbing *et al.* 2014; Bouman *et al.* 2015). Recently, Panet *et al.* (2014) analysis has demonstrated the sensitivity of these new data to lower mantle structure, which arises from the symmetries between the gradiometric differentiation directions and the global north–south/east–west organization of Earth's deep mass structure. The gradients improve geometry and depth information as compared to geoid data. For example, remnant slabs in the upper part of the lower mantle below North America, and in the

mid-lower mantle below Central Asia may be detected in the east–west gradients, and the subducted lithosphere related to the Tethys ocean closure, in the north–south gradients. This high sensitivity of gradients to the geometry of the masses opens new possibilities for investigating the dynamics of the mantle from global to regional scales by combining the gravity gradients with seismic tomography. Joint inversion of the observed geoid and seismic velocities has been commonly used to constrain the viscosity profile within the mantle as well as the lateral density variations. The main uncertainty is the relationship between seismic velocity and density, the so-called density/velocity scaling factor, because of the large number of effects that occur in these velocity variations, particularly temperature and chemical composition. Indeed, seismic anomalies caused by a combination of thermal and compositional effects cannot be simply converted to density anomalies. But because these compositional variations are probably most prominent at lithosphere depth—where the contribution of the associated density anomalies to the long-wavelength geoid are probably smaller than those at greater depth—we assume that the approach of a velocity–density scaling factor may be acceptable. Space gravimetry provides independent information, complementary to seismology, to image the structure of the mantle mass anomalies, and therefore the associated changes in temperature and composition. Since the pioneering studies for inferring the mantle structure from gravimetric data (e.g. Hager 1984; Ricard *et al.* 1989; Forte *et al.* 1994), several works have focused on how seismically inferred mantle structure may be used to explain geodynamic data. On the one hand, some studies search for the radial viscosity profile which fit the geoid and free-air gravity assuming a conversion factor (e.g. Soldati *et al.* 2009), or using constraints from mineral physics (Steinberger & Calderwood 2006). On the other hand, other authors fix the viscosity profile from Glacial Isostatic Adjustment (GIA) data (sea-level change for the past 20 kyr, present-day rate of surface vertical displacements and of the geoid, secular drift of the Earth’s rotational axis, etc.) and derive the conversion factor which explains the geoid, the free-air anomaly, the dynamic topography as well as the non-hydrostatic flattening of the core–mantle boundary (Forte 2007; Simmons *et al.* 2009). Marquart *et al.* (2005) proposed a joint estimation of the viscosity and the scaling factor profiles taking into account the mantle density distribution deduced from a slab subduction history model (Ricard *et al.* 1993) and an *S*-wave tomography model. Lateral variations in mantle rheology (Moucha *et al.* 2007), as well as density jumps at the transition zone discontinuities (Kaban & Trubitsyn 2012) have also been investigated.

Here we investigate how the gravity and the gradients of gravity data can provide new informations on the radial profile of viscosity and on the mantle mass anomalies.

The paper is organized as follows. In Section 2, we present our theoretical approach. In Section 3, we estimate the viscosities and the scaling factor for a two-layer and a three-layer mantle, with an heterogeneity structure given by the tomographic model S40RTS (Ritsema *et al.* 2011); we discuss the sensitivity of the method as a function of the number of layers within the mantle. In Section 4, these estimations are done for a four-layer mantle model using two different tomographic models: S40RTS, and the recent tomographic model SEMUCB-WM1 (French & Romanowicz 2014); the fit between the models and the observations is discussed. We present the geoid, the components of the gravity and of the gravity gradients for the best models and we discuss our results and especially the discrepancies between computed and observed data. In Section 5, to complete our study, we use a simple geodynamic model for the large-scale pattern of mantle mass anomalies derived from slab sub-

duction history and we jointly estimate the viscosity profile and the depth-dependent density contrast between the slabs and the surrounding mantle which provide the best fit between the models and the observations.

## 2 THEORETICAL APPROACH

### 2.1 Model

The distribution of the lateral variations of the density anomalies  $\delta\rho$  within the mantle is deduced from an *S*-wave tomography model. A major issue arises from the uncertainties in the relationship between seismic velocity and density. Theoretical mineral physics estimates are usually based on temperature effects alone, despite the fact that compositional effects may be important (for a review, see Forte 2007). Thermally induced density variations together with mineral phase changes and possible chemical differentiation favour a depth-dependent scaling factor (Forte & Perry 2000; Forte *et al.* 2002).

We denote the scaling or conversion factor as  $c(r) = \left(\frac{d \ln \rho}{d \ln V_s}\right)$ , with  $r$  the radius, such that:

$$\frac{\delta\rho(r, \theta, \varphi)}{\rho(r)} = c(r) \frac{\delta V_s(r, \theta, \varphi)}{V_s(r)} \quad (1)$$

where  $\rho(r)$  and  $V_s(r)$  are, respectively, the radial profile of density and of shear velocity and  $\delta V_s(r, \theta, \varphi)$  represents the shear velocity anomalies (i.e. the lateral variations with respect to the radial profile).  $\theta$  is the geocentric colatitude and  $\varphi$  the longitude.

We expand the density anomalies, at each depth, on the basis of the spherical harmonic functions  $Y_n^m(\theta, \varphi)$ , normalized to  $4\pi$ :

$$\delta\rho(r, \theta, \varphi) = \sum_{n,m} \delta\rho_n^m(r) Y_n^m(\theta, \varphi)$$

The total gravitational potential outside the Earth is:

$$W(r, \theta, \varphi) = U(r, \theta) + V(r, \theta, \varphi) \quad (2)$$

where  $U(r, \theta)$  is the gravitational potential of an idealized elliptical, rotating Earth model, at hydrostatic equilibrium, with the radial profile of density  $\rho(r)$  and  $V(r, \theta, \varphi)$  the perturbation of the gravitational potential induced by the lateral mantle mass anomalies.

Because the mantle is not rigid, these mass anomalies involve internal mass redistributions and associated surface readjustments that have to be taken into account in the computation of the gravitational potential, in addition to the direct effect of the mass (Richards & Hager 1984). The perturbation of the gravitational potential outside the Earth is:

$$V(r, \theta, \varphi) = \sum_{n,m} \left(\frac{a}{r}\right)^{n+1} V_n^m(a) Y_n^m(\theta, \varphi) \quad (3)$$

where  $a$  is the semi-major axis of the ellipsoidal Earth.  $V_n^m(a)$  are the coefficients of the spherical harmonics expansion of the surface gravitational potential induced by the mantle mass anomalies. Because the hydrostatic flattening induced by the rotation is small [ $\sim \frac{1}{300} \ll 1$ ], the deformations induced by the mass anomalies are computed as perturbations with respect to a spheroidal reference shape. Consequently, to compute the  $V_n^m(a)$  coefficients, we use a ‘degree  $n$  geoid kernel’, that is to say a transfer function between the degree  $n$  coefficients of the spherical harmonics expansion of the mantle mass anomaly  $\delta\rho_n^m$  and that of the gravitational potential  $V_n^m(a)$  (Richards & Hager 1984).

$$V_n^m(a) = \frac{4\pi Ga}{2n+1} \int_{\text{CMB}}^a G_n(r) \delta\rho_n^m(r) dr \quad (4)$$

where  $G_n(r)$ , the degree  $n$  geoid kernel, depends on the geometrical and physical properties of the spherical reference Earth, comprising here a constant density mantle and core and a depth-dependent viscosity  $\nu(r)$ .

Because we neglect the lateral variations in the viscosity and scaling factor profiles, we can only investigate the long-wavelength mantle density anomalies, and consequently we will take into account only the degrees ranging from 2 up to 20 in our analysis.

We work in a local reference frame, where  $X$  is the southward axis,  $Y$  the eastward one and  $Z$  the upward one (right-handed frame). Its origin is at the observation point and the coordinate system associated with it is the spherical coordinate system  $(r, \theta, \varphi)$  (e.g. Casotto & Fantino 2009).

The three components of the gravity vector induced by the mantle mass anomalies  $\vec{g} = -\vec{\nabla}V$ , in this local frame, may be written as:

$$V_Z = -\partial_r V \quad V_X = -\frac{1}{r}\partial_\theta V \quad V_Y = -\frac{1}{r\sin\theta}\partial_\varphi V \quad (5)$$

The nine components of the Eötvös tensor, that is to say the gradients of the gravity vector, induced by the mantle mass anomalies, may be written as (Koop 1993):

$$\begin{aligned} V_{ZZ} &= \partial_{rr}^2 V & V_{XX} &= \frac{1}{r} \left( \frac{\partial_{\theta\theta}^2 V}{r} + \partial_r V \right) \\ V_{YY} &= \frac{\partial_{\varphi\varphi}^2 V}{r^2 \sin^2 \theta} + \frac{\partial_r V}{r} + \frac{\cot\theta \partial_\theta V}{r^2} \\ V_{ZX} &= \frac{1}{r} \left( -\partial_{r\theta}^2 V + \frac{\partial_\theta V}{r} \right) & V_{ZY} &= \frac{1}{r\sin\theta} \left( \partial_{r\varphi}^2 V - \frac{\partial_\varphi V}{r} \right) \\ V_{XY} &= \frac{1}{r^2 \sin\theta} (\cot\theta \partial_\varphi V - \partial_{\theta\varphi}^2 V); & V_{YX} &= V_{XY}; \\ V_{XZ} &= V_{ZX}; & V_{YZ} &= V_{ZY} \end{aligned} \quad (6)$$

For given lateral density variations, the surface geoid, the gravity and the gravity gradients at the altitude of the GOCE satellite (about 255 km) may be computed, from these formulae, using the geoid kernels associated to the chosen viscosity profiles.

We assume a radially layered incompressible mantle model with viscosity and conversion factor constant in each layer, and we fix the viscosity of the lithosphere. From mineral physics studies (Karato & Karki 2001; Cammarano *et al.* 2003, 2005; Stixrude 2007) as well as from a geodynamics study (Marquart *et al.* 2005) or joint geodynamic and mineral physics studies (Steinberger & Calderwood 2006; Forte 2007), the full range of possible values for the scaling factor appears to be comprised between 0 and 0.4. Viscosity profiles within the mantle are constrained from geophysical data sensitive to the long-term rheology of the mantle: studies of postglacial uplift (e.g. Mitrovica 1996) constrain the absolute value of the viscosity, whereas studies of steady-state geoid associated with mantle convection constrain the relative variations of the viscosity with depth (Kaufmann & Lambeck 2000; Forte 2007). From these results, we assume that the viscosity of the upper mantle ranges from  $10^{19}$  to  $10^{21}$  Pa s while that of the lower mantle is between  $10^{21}$  and  $10^{24}$  Pa s.

Within these limits, we perform a Monte Carlo search for the viscosity and the density/velocity scaling factor profiles within the mantle which allow us to fit the observed geoid, gravity and gravity gradients.

## 2.2 Data

Our data are global maps of the non-hydrostatic surface geoid, and gravity and gravity gradients at satellite altitude. We have built these maps from models based on different data sets (CHAMP, GRACE and GOCE) in order to obtain if possible, independent datasets:

(1) For the non-hydrostatic surface geoid, we use the coefficients, up to degree 20, of the spherical harmonics expansion of the geoid derived from CHAMP (EIGEN-CHAMP05S model; Flechtner *et al.* 2010). The long-wavelength information from GRACE/LAGEOS is superior to the CHAMP-derived long-wavelength information, but the difference is very small as compared to the amplitude of the large-scale mantle structure signal studied here.

(2) For the gravity, we use the combined gravity field model EIGEN-GL04C (using coefficients, up to degree 20, of the spherical harmonics expansion of the geoid), which is obtained from a combination of GRACE and LAGEOS missions observations plus  $0.5^\circ \times 0.5^\circ$  gravimetry and altimetry surface grids (Foerste *et al.* 2008).

(3) For the gravity gradients, we use the global grids at 255 km height above the reference ellipsoid (WGS84), (available from [ftp.dgfi.badw.de/pub/goce2/Gradient-Grids](http://ftp.dgfi.badw.de/pub/goce2/Gradient-Grids)) (Bouman *et al.* 2013) which combine GRACE with GOCE data. Note that our data sets are then not fully independent.

For the scales up to degree 20 that are used here, it makes very little difference by which mission and which method the gravity field was obtained, when compared to the amplitude of the studied signals. So, at this level of accuracy, the gravity field coefficients up to degree 20 will be very similar for all three, and gradients and second derivatives may be obtained with eqs (5) and (6). Nevertheless we choose to use these global grids instead of deriving the gradients from the coefficients of the spherical harmonics expansion of the observed geoid.

We construct maps referring to an idealized elliptical, rotating Earth model, at hydrostatic equilibrium, with internal structure given by the PREM model deduced from seismology (Nakiboglu 1979, 1982; Dziewonski & Anderson 1981; Chambat *et al.* 2010) with the gravity potential  $U(r, \theta)$  introduced in eq. (2). An important consequence is that our non-hydrostatic geoid will differ at even degrees and order 0 from the reference geoid classically associated to the WGS84 ellipsoid used by geodesists. Our reference model is centred at the centre of mass and the mass of the Earth is conserved. Consequently, the degrees 0 and 1 coefficients of the spherical harmonics expansion of the non-hydrostatic potential are zero (for more details about degree one deformations, see Greff-Lefftz *et al.* 2010).

The gravity gradients are given on global grids with a constant step size of  $0.2^\circ$  for the geographic coordinates. Consequently, for our computation, we use the ellipsoidal coordinates instead of the spherical ones. We denote the radius of our reference ellipsoid as  $r_E$ :

$$r_E(\Psi, \varphi) = a \frac{\sqrt{1 + (e^4 - 2e^2) \sin^2 \Psi}}{\sqrt{1 - e^2 \sin^2 \Psi}} \quad (7)$$

where  $e$  is the eccentricity [ $e^2 = 1 - \frac{b^2}{a^2}$ ], with  $b$  the semi-minor axis of the ellipsoidal Earth and  $\Psi$  the geodetic latitude, which is related to the eccentricity and geocentric colatitude as:

$$\tan \Psi = \frac{1}{(1 - e^2) \tan \theta}$$

The gravitational potential  $V^{\text{obs}}$  will be plotted on this hydrostatic reference ellipsoid, that is, at  $r = r_E$ . Its mean value is:

$$\overline{V^{\text{obs}}} = \frac{1}{S_E} \int_0^{2\pi} \int_{-\pi/2}^{\pi/2} V^{\text{obs}}(r_E, \Psi, \varphi) dS \quad (8)$$

with  $dS = \frac{(1 - e^2) \cos \Psi}{1 - e^2 \sin^2 \Psi} d\Psi d\varphi$  and

$$S_E = \int_0^{2\pi} \int_{-\pi/2}^{\pi/2} dS = 2\pi \left[ 1 + \frac{1 - e^2}{2e} \ln \left( \frac{1 + e}{1 - e} \right) \right]$$

The gravity and the gradients are computed on the global grids derived by Bouman *et al.* (2013), that is to say at the altitude  $h$  above our hydrostatic reference ellipsoid, a surface with radius  $r_h$  related to the radius of the reference ellipsoid as:

$$r_h(\Psi, \varphi) = \frac{(a + h)}{a} r_E(\Psi, \varphi) \quad (9)$$

and the mean values over this surface are, for example, for  $V_{XX}$ :

$$\overline{V_{XX}^{\text{obs}}} = \frac{1}{S_E} \int_0^{2\pi} \int_{-\pi/2}^{\pi/2} V_{XX}^{\text{obs}}(r_h, \Psi, \varphi) dS \quad (10)$$

On the same surfaces, we can compute the standard deviation  $\sigma_{\text{data}}$ . For example, for the gravitational potential, at  $r = r_E$  and the  $V_{XX}$  component of the gravity gradient at  $r = r_h$ :

$$\sigma_V^2 = \frac{1}{S_E} \int_S [V^{\text{obs}}(r_E, \Psi, \varphi)]^2 dS - \overline{V^{\text{obs}}}^2; \quad (11)$$

$$\sigma_{V_{XX}}^2 = \frac{1}{S_E} \int_S [V_{XX}^{\text{obs}}(r_h, \Psi, \varphi)]^2 dS - \overline{V_{XX}^{\text{obs}}}^2$$

We have  $N = 10$  data sets, hereafter noted  $X_i(r, \Psi, \varphi)$ , for  $i = 1, \dots, N$ : the surface geoid  $X_1(r_E, \Psi, \varphi) = \frac{V^{\text{obs}}(r_E, \Psi, \varphi)}{g_0}$  where  $g_0$  is the gravity of the reference sphere, the three components of the gravity vector [ $X_2(r_h, \Psi, \varphi) = V_X^{\text{obs}}(r_h, \Psi, \varphi)$ ,  $X_3(r_h, \Psi, \varphi) = V_Y^{\text{obs}}(r_h, \Psi, \varphi)$ ,  $X_4(r_h, \Psi, \varphi) = V_Z^{\text{obs}}(r_h, \Psi, \varphi)$ ] and the six components of the gravity gradients [ $X_5(r_h, \Psi, \varphi) = V_{ZZ}^{\text{obs}}(r_h, \Psi, \varphi)$ ,  $X_6(r_h, \Psi, \varphi) = V_{XX}^{\text{obs}}(r_h, \Psi, \varphi)$ ,  $X_7(r_h, \Psi, \varphi) = V_{YY}^{\text{obs}}(r_h, \Psi, \varphi)$ ,  $X_8(r_h, \Psi, \varphi) = V_{ZX}^{\text{obs}}(r_h, \Psi, \varphi)$ ,  $X_9(r_h, \Psi, \varphi) = V_{ZY}^{\text{obs}}(r_h, \Psi, \varphi)$ ,  $X_{10}(r_h, \Psi, \varphi) = V_{XY}^{\text{obs}}(r_h, \Psi, \varphi)$ ].

These  $N$  data sets are not independent, so we also compute their covariance matrix. We note  $\overline{X_i}$  the expected value of the data  $X_i(r, \theta, \varphi)$ , defined by:

$$\overline{X_i} = \frac{1}{S_E} \int_0^{2\pi} \int_{-\pi/2}^{\pi/2} X_i(r, \Psi, \varphi) dS \quad (12)$$

and consequently

$$\overline{X_i X_j} = \frac{1}{S_E} \int_0^{2\pi} \int_{-\pi/2}^{\pi/2} X_i(r, \Psi, \varphi) X_j(r, \Psi, \varphi) dS \quad (13)$$

where  $r$  stands for  $r_E$  or  $r_h$ , following the data.

The elements of the  $10 \times 10$  covariance matrix over the data, noted  $C^D$ , are then:

$$C_{ij}^D = \overline{X_i X_j} - \overline{X_i} \overline{X_j} \quad (14)$$

Note that diagonal elements are the variances computed in (eq. 11). If the  $N$  data sets are independent, this matrix will be diagonal. The mean value  $\overline{X_i}$ , the standard deviation  $\sigma_{X_i}$  as well as the elements of the covariance matrix  $C_{ij}^D$  are given in Appendix A.

Note that, in this paper, the geoid will always be computed on the hydrostatic reference ellipsoid ( $r = r_E$ ), whereas the gravity and the gravity gradient will be computed at the altitude  $h$  above this ellipsoid ( $r = r_h$ ).

### 2.3 Measure of the fit between model and data

We measure the quality of the fit between the surface modeled versus observed geoid, and between the modeled gravity and gradients and the observed ones at the satellite altitude  $h$  using  $N = 10$  variance reduction estimates  $\Phi^{\text{data}}$ :

$$\Phi^{\text{Geoid}} = \left[ 1 - \frac{\frac{1}{S_E} \int_S (V^{\text{obs}}(r_E, \Psi, \varphi) - V^{\text{mod}}(r_E, \Psi, \varphi))^2 dS}{\sigma_V^2} \right] \quad (15)$$

$$\Phi^{V_Z} = \left[ 1 - \frac{\frac{1}{S_E} \int_S (V_Z^{\text{obs}}(r_h, \Psi, \varphi) - V_Z^{\text{mod}}(r_h, \Psi, \varphi))^2 dS}{\sigma_{V_Z}^2} \right] \quad (16)$$

and, for example,  $\Phi^{V_{XX}}$ :

$$\Phi^{V_{XX}} = \left[ 1 - \frac{\frac{1}{S_E} \int_S (V_{XX}^{\text{obs}}(r_h, \Psi, \varphi) - V_{XX}^{\text{mod}}(r_h, \Psi, \varphi))^2 dS}{\sigma_{V_{XX}}^2} \right] \quad (17)$$

Consequently, if a variance reduction  $\Phi^{X_i} = 1$ , it means that 100 per cent of the observed data  $X_i$  satisfy the model predictions.

## 3 JOINT ANALYSIS BASED ON SEISMIC TOMOGRAPHY: SENSITIVITY OF THE METHOD

In this section, we assess the sensitivity of the gravity potential, gravity and gravity gradients to mantle viscosity and velocity–density scaling factor. We estimate the viscosity profile and the scaling factor for a two-layer or a three-layer mantle model, starting from the coefficients of the spherical harmonics expansion, up to degree 20, of the  $S$ -wave tomography model S40RTS, derived by Ritsema *et al.* (2011). We test two simple Earth models: the classical two-layer mantle with an upper mantle and a lower mantle, and then a three-layer mantle in which we divide the lower mantle into two parts. When we increase the number of layers in the mantle, we increase the number of parameters that have to be estimated: from four parameters for the two-layer mantle, to six parameters for the three-layer mantle. The quality of the estimation of these parameters will be discussed.

### 3.1 Two-layer mantle and S40RTS tomographic model

We first test a two-layer mantle, that is to say a viscous Earth model with a 100 km thick lithosphere, an upper mantle (100–670 km), a lower mantle (670–2891 km) and an inviscid fluid core. Because studies of steady-state gravity functionals associated with mantle convection only constrain the relative variations of the viscosity with depth, we set the value of the viscosity of the lithosphere: we arbitrary choose a value of about  $\nu_1 = 1.1 \times 10^{22}$  Pa s, a value obtained by Ricard *et al.* (1993) from a joint inversion of mantle density heterogeneities based on slab history and the geoid. Ricard *et al.* (2006) investigated the crustal and lithospheric sources of the gravity field and showed that for the lowest degrees, the isostatically compensated crustal and lithospheric signal is much lower in amplitude than the mantle one. Consequently, we neglect this lithospheric contribution, that is to say we assume that the scaling factor within the lithosphere is equal to zero. We note, respectively,  $\nu_2$  ( $\nu_3$ ) and  $c_2$  ( $c_3$ ) the viscosity and the scaling factor of the upper mantle (lower mantle).

For realistic values of the viscosity—between  $10^{19}$  and  $10^{23}$  Pa s—and upper and lower limits 0–0.4 for the conversion

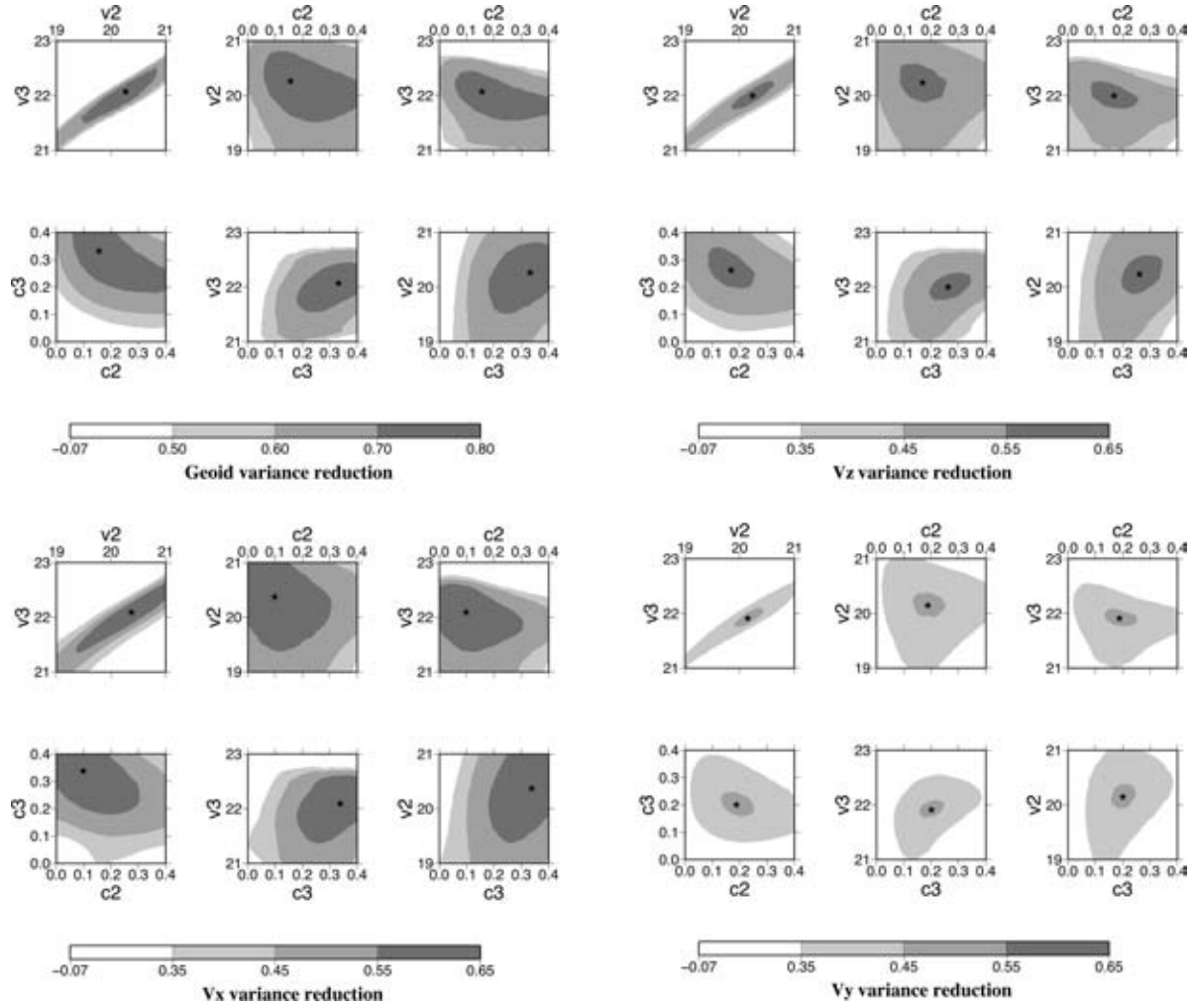


**Figure 1.** Variance reduction for the surface geoid and for the gravity at the altitude of the GOCE satellite.

factor, we have performed a Monte Carlo search for these four parameters and more than  $2.56 \times 10^6$  different combinations of  $c_2$ ,  $v_2$ ,  $c_3$  and  $v_3$  have been calculated. For each type of data, we have obtained a four-variable function for the variance reduction, such as  $\Phi^{\text{Geoid}}(c_2, c_3, v_2, v_3)$ . Because we cannot plot a 4-D function, we compute, for each pair of parameters, the maximum value of the variance reduction obtained for all other parameters. For example, for the geoid variance reduction, we plot at the top left of Fig. 1(a) the function  $f(v_2, v_3) = \text{Max}_{c_2, c_3} \Phi^{\text{Geoid}}(c_2, c_3, v_2, v_3)$ . The darkest grey surface of the curve corresponds to the values of the parameters ( $v_2, v_3$ ) leading to a variance reduction for the geoid greater than 0.7, that is to say with more than 70 per cent of the observed surface geoid data satisfying the model predictions. Note that there is a large range of possible values for the viscosities: nevertheless, the ratio  $v_3/v_2$  remains constant and is determined to a value of about 50. The black star in the figure corresponds to the best model for the geoid.

We plot similar curves for the three components of the gravity at the satellite altitude (Figs 1b–d) and for the six components of the gradients of gravity at the satellite altitude (Fig. 2). For the gravity vector, the best variance reduction is obtained for the north–south component  $V_x$  whereas it is always smaller for the east–west component  $V_y$ . For the gradients of gravity, the variance reduction exceeds 0.3 only for  $V_{zz}$ ,  $V_{xx}$  and  $V_{zx}$ . All components with longitude derivative exhibit weaker variance reduction. This may be explained by

the lack of north/south structures in the tomographic model. Indeed, comparisons between different seismic tomography models found in the literature show a discrepancy between these various velocity perturbations in the region between 420 and 1150 km (Lee *et al.* 2011), a zone where remnant slabs may be present, for example, below North America (see Section 5).

We compute 10 best models obtained for each data set and we plot in Fig. 3 the obtained values for the scaling factor and for the viscosity. Note that whatever the data set, the best fit is obtained for similar values of viscosities and the viscosity ratio remains close to 50. This is not the case for the scaling factors which seem larger when obtained from the geoid and the gravity than from the gradients of gravity, probably because they are sensitive to structures at different depth; however  $c_3 > c_2$  for all the data.

To reconcile these 10 best models into a single best model, we combine the informations from these different data sets using a probability function  $p(c_2, c_3, v_2, v_3)$  defined by:

$$p(c_2, c_3, v_2, v_3) = \exp \left[ -\frac{1}{2} \sum_{i=1}^N \sum_{j=1}^N \frac{1}{S_E} \times \int_0^{2\pi} \int_{-\pi/2}^{\pi/2} (X_i^{\text{mod}} - X_i^{\text{obs}}) C_{ij}^{D-1} (X_j^{\text{mod}} - X_j^{\text{obs}}) dS \right] \quad (18)$$

with  $N = 10$ ,  $C^D$  being the covariance matrix defined in (14).

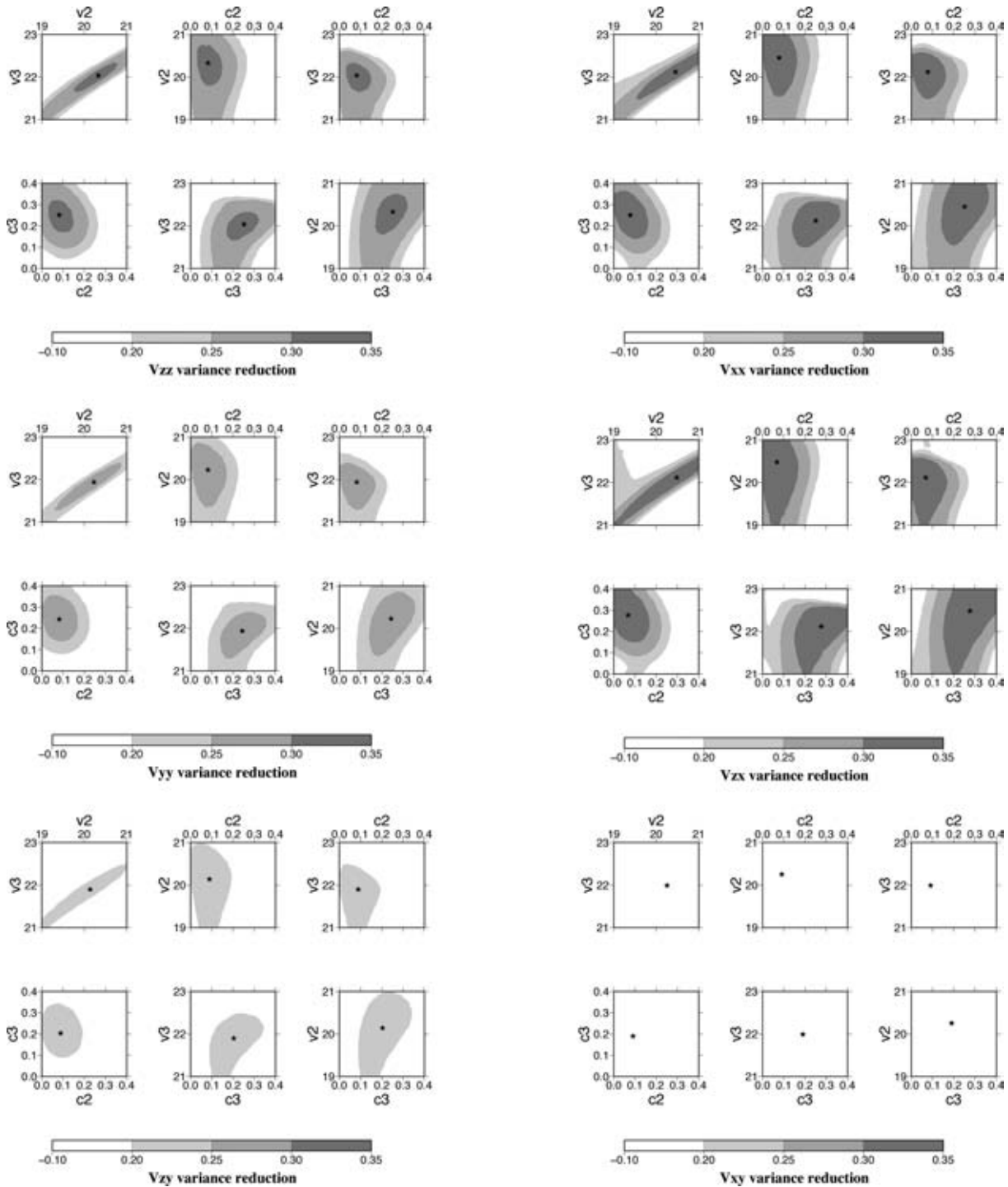


**Figure 2.** Variance reduction for the six components of the gravity gradient at the altitude of the GOCE satellite.

The values of the parameters obtained for the maximum probability are given in Table 1 (column ‘Best model’) and are plotted as a dashed line in Fig. 3. The viscosity estimates for each single data set do not differ much and are close to the values obtained for the maximal probability. This is not true for the scaling factors which show a large dispersion, especially in the lower mantle.

The  $N$  variance reductions  $\Phi^{\text{data}}$  associated with this best model are given in Table 6. The variation reduction  $\Phi^{\text{Geoid}}$  associated with

the best model obtained for the maximum probability is less than 0.7: this low value (in comparison with the large areas with geoid variance reductions in excess of 0.7 shown in Fig. 1) may be explained by the fact that the upper-mantle scaling factor determined using only geoid is about two times larger than the one obtained for the best model (Fig. 3).

In order to interpret our results, we compute the probability distribution of one parameter regardless of the other parameters, that is to say the marginal distribution. For example, the marginal

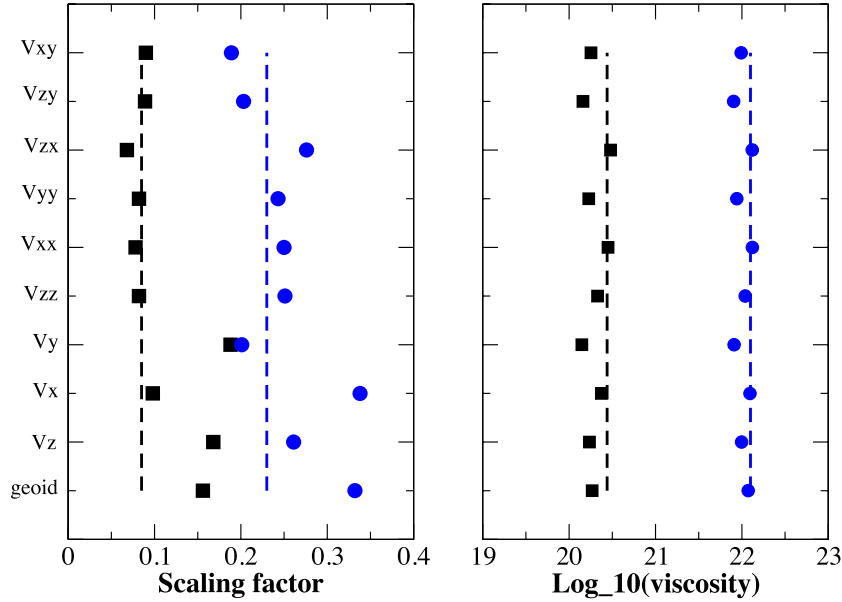


**Figure 3.** Estimates of the scaling factor (left) and of the viscosity (right) for the two-layer model. 10 best models obtained for each of 10 data sets:  $c_2$  as black square and  $c_3$  as black circle, on the left figure, and  $v_2$  as black square and  $v_3$  as black circle, on the right. Dashed line: best model obtained from the maximum probability.

**Table 1.** Scaling factor and  $\log_{10}$  (viscosity in Pa s) values for the two-layer mantle model: expected value and standard deviation computed from (20). Best model obtained from the maximum probability (eq. 18).

| Layer        | Scaling factor                                |            | $\log_{10}$ (Viscosity in Pa s)               |            |
|--------------|---|------------|---|------------|
|              | Expected value<br>$\pm$<br>standard deviation | Best model | Expected value<br>$\pm$<br>standard deviation | Best model |
| Upper mantle | $0.117 \pm 0.085$                             | 0.096      | $20.04 \pm 0.55$                              | 20.30      |
| Lower mantle | $0.168 \pm 0.101$                             | 0.233      | $21.86 \pm 0.41$                              | 22.03      |

distribution of  $c_2$  is simply the probability distribution of  $c_2$  integrating over information about  $c_3$ ,  $v_2$  and  $v_3$ .

$$\tilde{p}(c_2) = \frac{\int_{c_3} \int_{v_2} \int_{v_3} p(c_2, c_3, v_2, v_3) dc_3 dv_2 dv_3}{\int_{c_2} \int_{c_3} \int_{v_2} \int_{v_3} p(c_2, c_3, v_2, v_3) dc_2 dc_3 dv_2 dv_3} \quad (19)$$

We plot in Fig. 4(a) the marginal probability for the scaling factors (top, in black for  $c_2$ , in blue for  $c_3$ ) and for the viscosities (bottom, in black for  $v_2$ , in blue for  $v_3$ ).

We have divided the 4-D space of parameters into  $4 \times 20$  intervals. Our a-priori knowledge of one parameter is a uniform distribution in the explored interval: all the values have the same probability, equal to  $\frac{1}{20} = 0.05$  as we have divided each dimension into 20 intervals. The distribution that we get *a posteriori* (Fig. 4) represents the information obtained after inversion. So the more the marginal probability differs from a uniform distribution (0.05), the more information is gained.

The values of  $c_2$  and  $c_3$  obtained for the maximum probability ( $c_2 = 0.096$  and  $c_3 = 0.233$ , indicated with dashed lines in Fig. 4a) have a marginal probability of about 0.093 and 0.054, respectively.  $c_3$  is therefore not well estimated because the marginal probability is only slightly larger than the uniform probability of 0.05. For the viscosity, the marginal probability is equal to 0.057 for  $\log_{10}(v_2) = 20.30$  and 0.089 for  $\log_{10}(v_3) = 22.03$ . According to the curve

shapes, we can conclude that the viscosity of the lower mantle is better estimated than that of the upper mantle, in our joint inversion.

To quantify the accuracy of this estimation, we compute the standard deviation of the parameters  $c_2$ ,  $c_3$ ,  $\log_{10}(v_2)$ ,  $\log_{10}(v_3)$ . If the random variable  $X$  is discrete with probability density function  $x_1 \rightarrow p_1, \dots, x_M \rightarrow p_M$ , then the standard deviation of  $X$  is the quantity  $\sigma_X$  such that:

$$\sigma_X = \sqrt{\frac{\sum_{i=1}^M p_i (x_i - \bar{x})^2}{\sum_{k=1}^M p_k}} \quad \text{with} \quad \bar{x} = \frac{\sum_{k=1}^M p_k x_k}{\sum_{k=1}^M p_k} \quad \text{the expected value.} \quad (20)$$

Note that these numbers may be partly dependent on the intervals chosen, especially for those cases where the marginal probability distribution remains close to 0.05.

The obtained values for the scaling factor and for the  $\log_{10}$  of the viscosities are given in Table 1. Note that our best model is within the error bars. Our procedure essentially gives different weighting (e.g. compared to only considering the geoid, or only vertical gravity) to different parts of the data set. So to estimate the relative importance

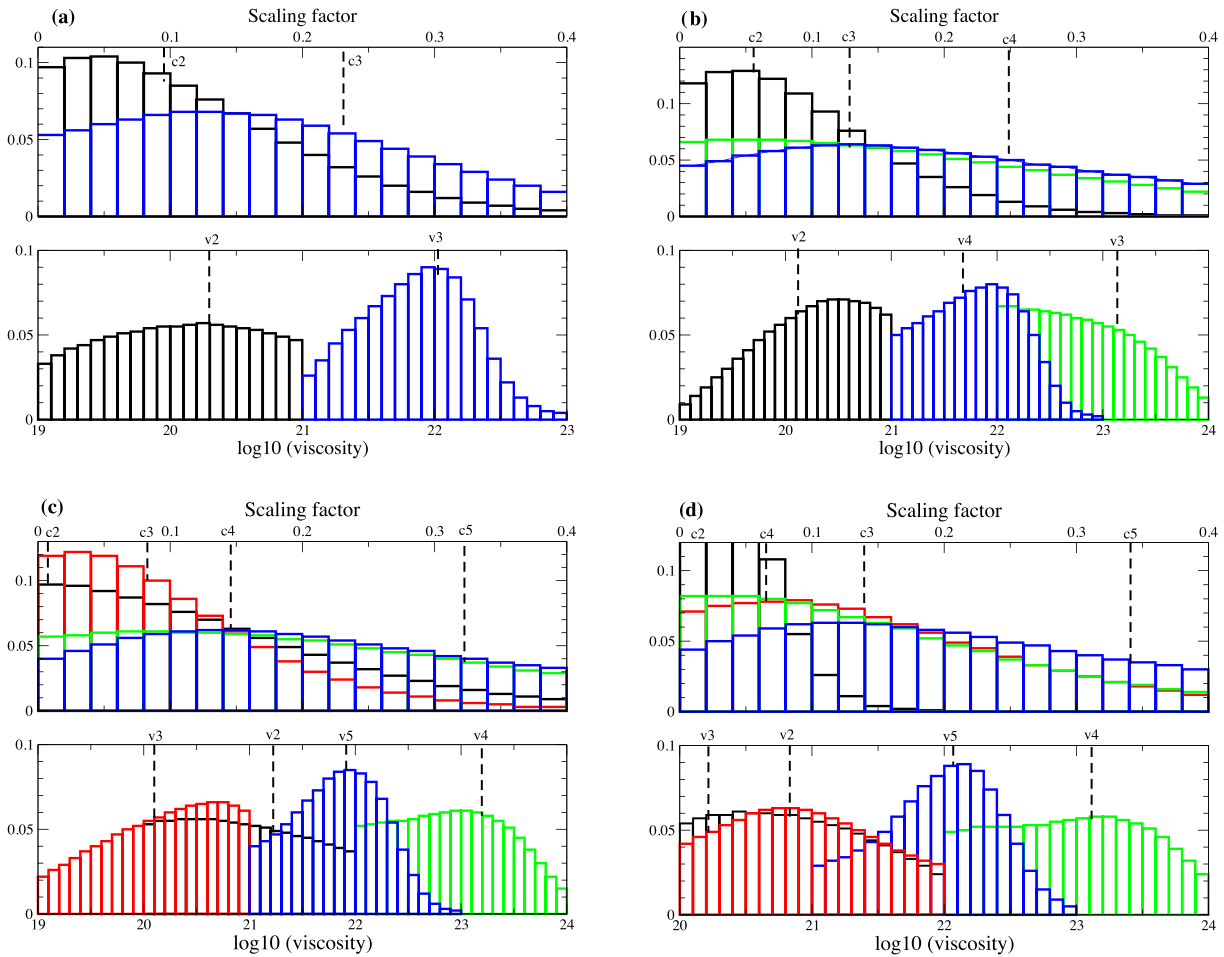


**Figure 4.** Marginal probability for the scaling factor (top) and for the viscosity (bottom) for the four mantle models discussed in the text: (a) two-layer mantle:  $c_2$  and  $v_2$  in black,  $c_3$  and  $v_3$  in blue, for S40RTS tomographic model. (b) Three-layer mantle:  $c_2$  and  $v_2$  in black,  $c_3$  and  $v_3$  in green,  $c_4$  and  $v_4$  in blue, for S40RTS tomographic model. (c) Four-layer mantle:  $c_2$  and  $v_2$  in black,  $c_3$  and  $v_3$  in red,  $c_4$  and  $v_4$  in green,  $c_5$  and  $v_5$  in blue, for S40RTS tomographic model (d) same as (c) for SEMUCB tomographic model. Note that the viscosity scale is different.

of each data, we compute 10 probability functions such as, for example, for the geoid:

$$p_{\text{geoid}}(c_2, c_3, v_2, v_3) = e^{-\frac{N(1-\Phi^{\text{Geoid}})}{2}} \quad (21)$$

The associated marginal probabilities are plotted in Fig. 5, top for the scaling factor and bottom for the viscosity. We find that the gradients of the gravity improve the estimate of the radially averaged scaling factor within the upper mantle—because they are sensitive to masses within the upper mantle—, whereas the geoid and the gravity better constrain that of the lower mantle. For the viscosity, we find that the probability functions are very similar, whatever the data used in the estimation: the geoid, the gravity and the gravity gradients depend on the dynamic topography, both at the surface and at the core–mantle boundary (Richards & Hager 1984) and consequently are sensitive to both upper and lower mantle viscosities.

### 3.2 Three-layer mantle and S40RTS tomographic model

To improve the fit between models and observations, we increase the number of layers within the mantle, that is to say the number of parameters that have to be estimated. In this part, we test a three-

layer mantle: the upper mantle (100–670 km), a top layer of the lower mantle (670–1150 km) and the lowermost mantle (1150–2891 km). We denote the viscosity and scaling factor of the upper mantle, the top of the lower mantle and the bottom of the mantle as  $v_2$ ,  $v_3$ ,  $v_4$  and  $c_2$ ,  $c_3$ ,  $c_4$ .

We have performed a Monte Carlo search for these six parameters and more than  $18 \times 10^6$  different combinations of  $c_2$ ,  $v_2$ ,  $c_3$ ,  $v_3$ ,  $c_4$  and  $v_4$  have been calculated. We compute 10 variance reductions which are now functions of six parameters, and similarly to the previous section, we compute for each pair of parameters the maximum variance obtained for all the other parameters (Appendix B, Figs B1 and B2). We plot the values of the scaling factor and the viscosity, in Fig. 6, for the 10 best models obtained for each of 10 data sets. The values obtained for the maximum probability, (eq. 18) are plotted as a dashed line and reported in Table 2 in the column ‘Best model’. The  $N$  variance reductions  $\Phi^{\text{data}}$  associated with this best model are given in Table 6.

The viscosity estimates for single data sets do not differ much and are close to the values obtained for the maximal probability. This is not true for the scaling factors which show a large dispersion, especially in the lower mantle.

The expected values and the standard deviations obtained for the scaling factor and for the  $\log_{10}$  of the viscosity are given in Table 2.

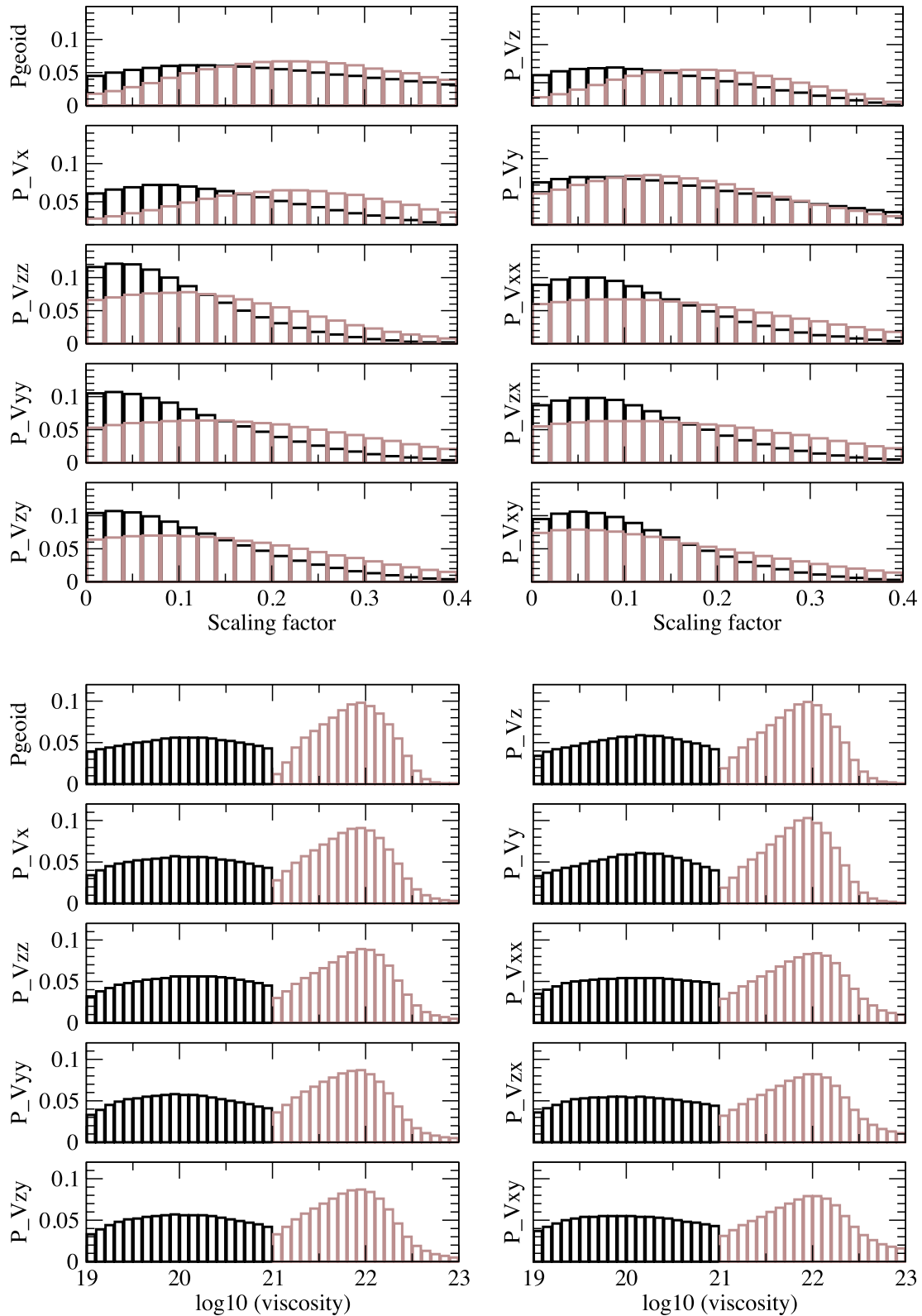


**Figure 5.** Marginal probability associated with each data sets, top for the scaling factor and bottom for the viscosity: upper-mantle parameter in black and lower mantle parameter in brown.

The marginal probability for the scaling factor and for the viscosity is plotted in Fig. 4(b).

From these results, we argue that it is not possible to robustly constrain with this method the scaling factor and the viscosity of

the layer 670–1150 km. As a matter of fact, we find, on the one hand, that the marginal probabilities for these two parameters are only slightly above 0.05 and consequently that they are not well determined in our inversion, and on another hand, that adding this

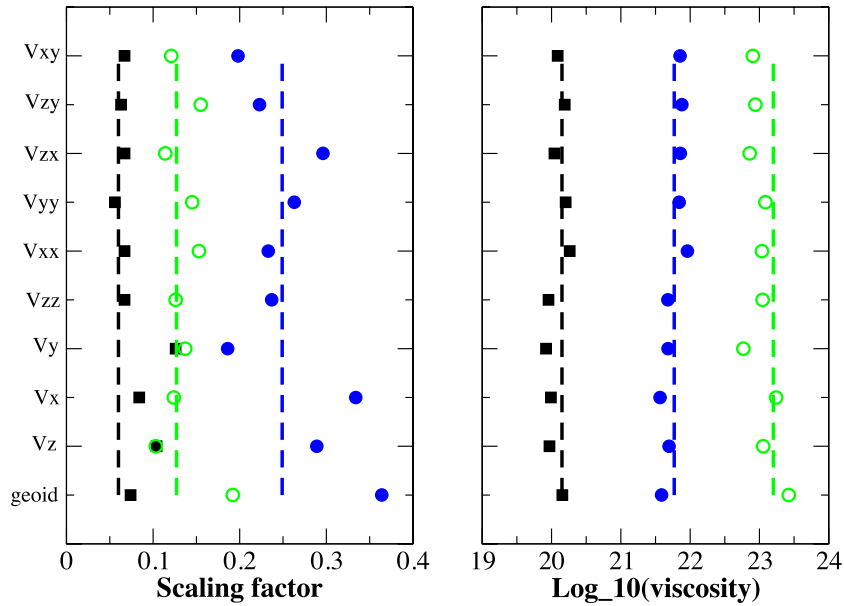


**Figure 6.** Estimates of the scaling factor (left) and of the viscosity (right) for the three-layered model. Best models obtained for each of 10 data:  $c_2$  as black square,  $c_3$  as green open circle and  $c_4$  as blue circle, on the left figure, and  $\nu_2$  as black square,  $\nu_3$  as green open circle and  $\nu_4$  as blue circle, on the right. Best models obtained from the maximum probability: dashed line.

**Table 2.** Same as Table 2 for a three-layer mantle.

| Layer        | Scaling factor                                |            | $\log_{10}$ (Viscosity in Pa s)               |            |
|--------------|---|------------|---|------------|
|              | Expected value<br>$\pm$<br>standard deviation | Best model | Expected value<br>$\pm$<br>standard deviation | Best model |
| Upper mantle | $0.094 \pm 0.069$                             | 0.060      | $20.21 \pm 0.50$                              | 20.15      |
| 670–1150 km  | $0.165 \pm 0.107$                             | 0.127      | $22.84 \pm 0.52$                              | 23.12      |
| 1150–2890 km | $0.182 \pm 0.107$                             | 0.249      | $21.78 \pm 0.43$                              | 21.77      |

670–1150 km layer does not seem to notably increase the variance reductions (see Fig. 1 and Appendix B).

#### 4 FINAL MODELS BASED ON SEISMIC TOMOGRAPHY FOR A FOUR-LAYER MANTLE

In this part, we will use two different four-layer mantle models starting from two different  $S$ -wave tomography models.

##### 4.1 Four-layer mantle and S40RTS tomographic model

We test a four-layer mantle consisting of a two-layer upper mantle (100–280 km and 280–670 km), and a two-layer lower mantle (670–1150 km and 1150–2891 km), and we use the S40RTS tomographic model. Thus, we only have one additional layer in the upper mantle compared with the three-layer model investigated in the previous section, and compared with the two-layer model, the upper and lower mantle have been split in two. We denote the viscosity and scaling factor of the four layers as  $\nu_2, \nu_3, \nu_4, \nu_5$  and  $c_2, c_3, c_4, c_5$ , respectively, from the top to the bottom of the mantle. We have performed a Monte Carlo search for these eight parameters and more than  $48 \times 10^6$  different combinations of  $c_2, \nu_2, c_3, \nu_3, c_4, \nu_4, c_5$  and  $\nu_5$  have been calculated.

We compute 10 variance reductions which are now functions of eight parameters, and similarly to the previous sections, we compute for each pair of parameters the maximum variance obtained for all the other parameters (Appendix B, Figs B3 and B4). As for the two- and three-layer mantle models, we find that all the components with longitude derivative involve weak variance reduction.

We plot the obtained scaling factors and viscosities in Fig. 7, for the 10 best models associated with each of 10 data sets. The values obtained for the maximum probability (eq. 18) are plotted as a dashed line for the upper mantle and as a dotted-dashed line for the lower mantle and reported in the column ‘Best model’ of Table 3. The  $N$  variance reductions  $\Phi^{\text{data}}$  associated with this best model are given in Table 6.

The marginal probabilities for the scaling factor and for the viscosity are plotted in Fig. 4(c): note that the marginal probability for the viscosity in the upper mantle and at the top of the lower mantle is very close to 0.05 and consequently the value of this parameter is not well estimated from our inversion. The expected values and standard deviations obtained for the scaling factor and for the  $\log_{10}$  of the viscosities are given in Table 3.

##### 4.2 Four-layer mantle and SEMUCB tomographic model

To improve our results, we change the upper-mantle stratification and we investigate the influence of the tomographic model.

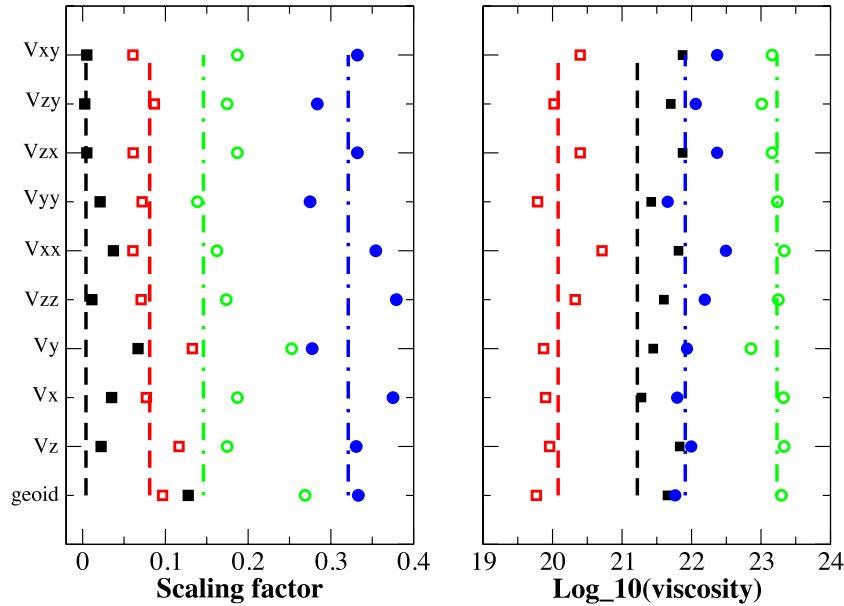


**Figure 7.** Estimates of the scaling factor (left) and of the viscosity (right) for the four-layered model for the S40RTS tomographic model. Best models obtained for each of 10 data:  $c_2$  as black square,  $c_3$  as red open square,  $c_4$  as green open circle and  $c_5$  as blue circle, on the left figure, and  $v_2$  as black square,  $v_3$  as red open square,  $v_4$  as green open circle and  $v_5$  as blue circle, on the right. Best models obtained from the maximum probability: dashed line for the upper mantle and dotted-dashed line for the lower mantle.

**Table 3.** Same as Table 2 for the four-layer mantle.

| Layer        | Scaling factor                                |            | $\log_{10}$ (Viscosity in Pa s)               |            |
|--------------|---|------------|---|------------|
|              | Expected value<br>$\pm$<br>standard deviation | Best model | Expected value<br>$\pm$<br>standard deviation | Best model |
| 100–280 km   | $0.130 \pm 0.095$                             | 0.004      | $20.94 \pm 0.56$                              | 21.22      |
| 280–670 km   | $0.103 \pm 0.078$                             | 0.081      | $20.16 \pm 0.53$                              | 20.08      |
| 670–1150 km  | $0.177 \pm 0.109$                             | 0.146      | $22.90 \pm 0.52$                              | 23.23      |
| 1150–2890 km | $0.188 \pm 0.107$                             | 0.321      | $21.83 \pm 0.42$                              | 21.91      |

We assume an upper mantle with two layers (100–420 km and 420–670 km) and a two-layer lower mantle (670–1150 km and 1150–2891 km). We perform a Monte Carlo search for the eight parameters  $v_2$ ,  $v_3$ ,  $v_4$ ,  $v_5$  and  $c_2$ ,  $c_3$ ,  $c_4$ ,  $c_5$ , the viscosity and the scaling factor of the four layers, for the recent tomographic model SEMUCB (French & Romanowicz 2014), taking into account the degrees ranging from 2 up to 20.

We compute 10 variance reductions, and, for each pair of parameters, the maximum variance obtained for all the other parameters (Appendix B, Figs B5 and B6). We obtain larger variance reductions for  $V_Y$ ,  $V_{YY}$ ,  $V_{ZY}$  and  $V_{XY}$ —the components with derivative with respect to the longitude—than the ones obtained for the  $S$ -wave tomography model S40RTS. This may be due to a better resolution of this recent SEMUCB model to longitudinal mass anomalies.

We plot the values of the scaling factors and of the viscosities in Fig. 8, for 10 best models obtained for each of 10 datasets. The values obtained for the maximum probability (eq. 18), are plotted as a dashed line for the upper mantle and as a dotted-dashed line for the lower mantle and reported in the column ‘Best model’ of Table 4. The  $N$  variance reductions  $\Phi^{\text{data}}$  associated with this best model are given in Table 6.

The marginal probability for the scaling factor and for the viscosity is plotted in Fig. 4(d). The obtained expected values and standard

deviations for the scaling factor and for the  $\log_{10}$  of the viscosities are given in Table 4.

### 4.3 Best models for a four-layer mantle

We plot in Fig. 9 the best four-layer models obtained for S40RTS (black line) and SEMUCB (red line) tomographic models: in solid line, when we use the maximum probability (eq. 18) to estimate the scaling factors and the viscosities (Best model in Tables 3 and 4).

There is no significant difference between these models for the viscosity profile. The viscosity decreases in the lower part of the upper mantle (about  $10^{20}$ – $2 \times 10^{20}$  Pa s) and increases in the upper part of the lower mantle (about  $10^{23}$  Pa s).

We now discuss the robustness of these results:

(1) The value of the viscosity in the upper part of the mantle ( $v_2$ ) obtained with the use of the maximum probability is quite surprising in comparison with the ones obtained using each single data: the black squares in the right-hand panel of Figs 7 and 8 do not cluster around the corresponding dashed line. It means that our best model for this parameter is not robust: the marginal probability for  $v_2$  is a quasi-uniform distribution, close to 0.05 (Figs 4c and d), meaning that any value is almost as likely as another.

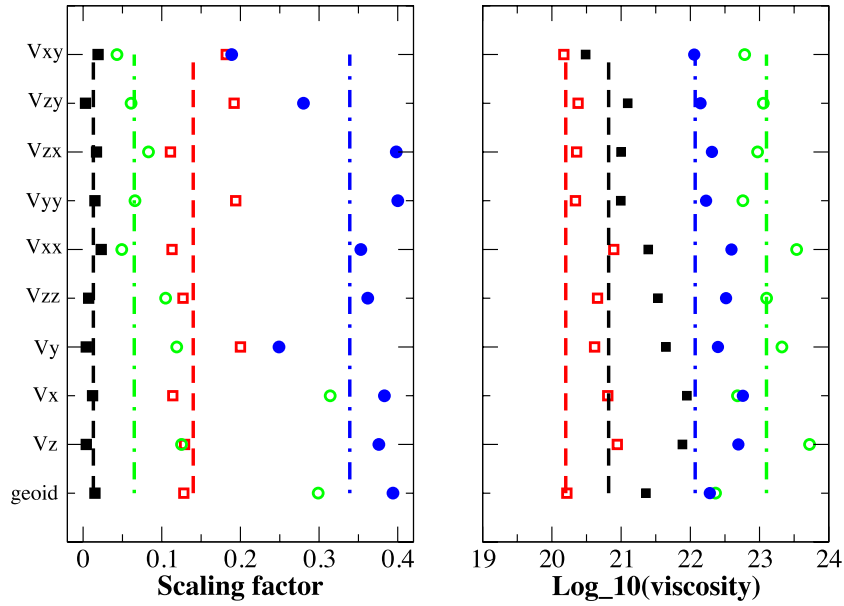


Figure 8. Same as in Fig. 7 for the SEMUCB tomographic model.

Table 4. Same as in Table 4 for the tomographic model SEMUCB (French & Romanowicz 2014) and for another upper-mantle stratification.

| Layer        | Scaling factor                            |            | log <sub>10</sub> (Viscosity in Pa s)     |            |
|--------------|---|------------|---|------------|
|              | Expected value<br>±<br>standard deviation | Best model | Expected value<br>±<br>standard deviation | Best model |
| 100–420 km   | 0.038 ± 0.030                             | 0.013      | 20.89 ± 0.54                              | 20.82      |
| 420–670 km   | 0.147 ± 0.098                             | 0.140      | 20.25 ± 0.52                              | 20.20      |
| 670–1150 km  | 0.145 ± 0.101                             | 0.065      | 22.96 ± 0.54                              | 23.10      |
| 1150–2890 km | 0.183 ± 0.107                             | 0.339      | 21.96 ± 0.44                              | 22.07      |

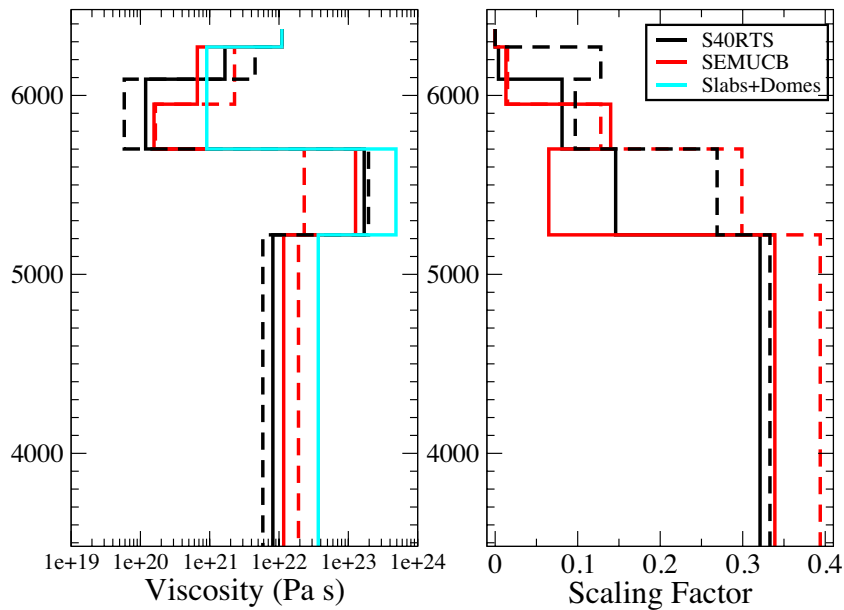


Figure 9. Estimates for the viscosity (left figure) and for the scaling factor (right figure) obtained for S40RTS (black line) and SEMUCB (red line) tomographic models: (1) solid line: scaling factor and the viscosity estimated from the maximum probability (best models in Table 4 and 5); (2) dashed line: scaling factor and the viscosity estimated from the geoid; (3) cyan line: viscosity estimated from the ‘Slabs+Domes’ model (Section 5).

(2) For both S40RTS and SEMUCB, the viscosity in the lower part of the upper mantle is less than in its upper part. But this feature is still controversial: Lee *et al.* (2011) taking into account the uncertainty variations in seismic model considered in the inversion process have argued that this is not a robust result.

(3) Similarly to the best model obtained for a three-layer mantle, we obtain that the large value of the viscosity of the 670–1150 km layer is not a robust feature, because the marginal probability for this viscosity has a rather broad maximum only slightly above 0.05 (see green plots on Figs 4b–d).

(4) The viscosity of the lower mantle is well estimated in our Monte Carlo search and is about  $10^{22}$  Pa s.

Let us now discuss the consistency of our results with studies based on GIA. The Haskell constraint on the average mantle viscosity, revisited by Mitrovica (1996), is about  $0.65\text{--}1.1 \times 10^{21}$  Pa s where the average resolved by the data encompasses a region which extends from the base of the lithosphere to a depth near 1400 km. This constraint is based on the analysis of decay times associated with uplift at different sites near the centre of previously glaciated regions, which provide a measure of mantle viscosity independent on the uncertainties in the space–time history of the late Pleistocene ice sheets. This constraint has been limited to the Maxwell rheology to represent the mechanical behaviour of the mantle. Most of the studies on global scale GIA predict a relatively low value for the lower mantle viscosity, in contradiction with results derived here and from longer timescale geodynamic inversions. A recent study (by Caron, Métivier, Greff-Lefftz, Fleitout and Rouby, GJI, in revision) includes transient relaxation, via Burgers rheology, in global scale GIA calculations that invert for both ice history and rheological parameters. They address the importance of this transient response by comparing inversions using Maxwell and Burgers rheologies. Their Bayesian approach allows them to study the non-uniqueness of the GIA solutions, revealing a large trade-off effect between the lower mantle and ice distribution and two local maxima in the probability density function. One of them agrees with long-term mantle dynamics. Because of that, we think that the viscosity profile obtained in our Monte Carlo search is consistent with studies based on GIA.

In the upper part of the mantle, the scaling factor is low: it essentially means that seismic velocities and densities are mostly unrelated, the chemical density anomalies being presumably more prominent at shallow depths (less than 200 km). In the upper mantle, the scaling factor increases with depth and is well constrained (marginal probability around 0.1). In the lower mantle, it is larger in the lowest part with values larger than 0.3 for all the models. Within the layer 670–1150 km, the scaling factor  $c_4$  is strongly dependent on the *S*-wave anomalies models and on the data sets used in the inversion: its value is slightly smaller than the one of the immediately above layer for SEMUCB, whereas its value increases within depth for S40RTS. This may be explained by the differences between the two tomographic models in this zone. But keep in mind that its marginal probability is of about 0.06, slightly above 0.05.

To investigate the informations provided by the gravity data and by the gravity gradients data, we compare these best models with the ones obtained if we take into account only the geoid data in the estimation of the eight parameters (dashed black line for S40RTS and dashed red line for SEMUCB), in Fig. 9. All models are quite similar for the viscosity and for scaling factor in the lower part of the mantle, whereas larger differences are observed for the scaling

factor in the upper parts of the mantle, due to the informations provided by the gravity gradients.

#### 4.4 Geoid, gravity and gravimetric gradients for the best models

We compute and plot the geoid, and the three components of the gravity in Fig. 10 associated with the two best models described above (solid lines in Fig. 9), as well as the six components of the gravity gradient (Fig. 11), using only the coefficients of the spherical harmonics expansion of the seismic velocity up to degree 20. Note, at first glance, the good correlations between the calculated signal and the observed data (also plotted using only the coefficients of the spherical harmonics expansion of the gravitational potential up to degree 20). To investigate these results in more details, we plot, for the tomographic model S40RTS, the discrepancy between the observed and calculated geoid, gravity and gravity gradients, in Figs 12 and 13 (for a better visualization, the scale is different than those of Figs 10 and 11).

We now discuss how to explain some discrepancies between estimated models and observations. The Large Low Shear Velocity Provinces (LLSVP) at the bottom of the mantle generate two bumps in the geoid just above them (Richards & Engebretson 1992). The amplitude of the French Polynesia geoid anomaly is larger in the observations than in our model. The modeled geoid high over Africa is located in the southwest part of the continent whereas the observed one is in its northern part. This difference may be due to lateral variations of the scaling factor at the bottom of the mantle: the LLSVPs are thought to consist of thermochemical piles whereas the fast *S*-wave anomalies at the bottom of the mantle may be related to cold slabs. A unique conversion factor at the bottom of the mantle is thus not realistic, even for these large-wavelength anomalies (e.g. Tkalcic & Romanowicz 2002). This can also explain the underestimated geoid anomaly above India or above Siberia induced by remnants of subducted Jurassic lithosphere. Another cause of discrepancy is that the viscous rheology of our lithosphere (with the value of  $1.1 \times 10^{22}$  Pa s set for the viscosity in our model) is not valid at regional scale over cratons. Indeed a ‘soft’ lithosphere, which is necessary to explain the geoid at large wavelength, corresponds to an effective ‘soft’ viscosity in order to take into account plate tectonics. We also note significant differences at the oceanic ridges, for example, in the Atlantic ocean or in the Red Sea: lateral variations of the scaling factor should be introduced in the upper mantle to simultaneously explain the geoid over the old continents and over the young oceanic ridge. The differences corresponding to regions where postglacial rebound is important (white small circles in Figs 12 and 13) show the static contribution of GIA (Métivier & Greff-Lefftz 2012). A recent study (Métivier *et al.* 2015) investigates the question of a remaining GIA signal in the present-day static gravity field assuming different models of ice history and different viscosity profiles. The study points out the remarkable signature of the former ice sheets in the present-day gravity gradients. Consequently, mantle convection is not the only candidate to explain Laurentian, Fennoscandian and Antarctic anomalies in the gravitational data.

Finally, a comparison between the different seismic tomography models found in the literature shows discrepancies in the velocity perturbations as a function of depth, especially between 420 and 1150 km (Lee *et al.* 2011, their fig. 2a). This region seems not well constrained by seismic data. So, to investigate the sensitivity of the viscosity to the mass anomalies in this zone, we will use in the next

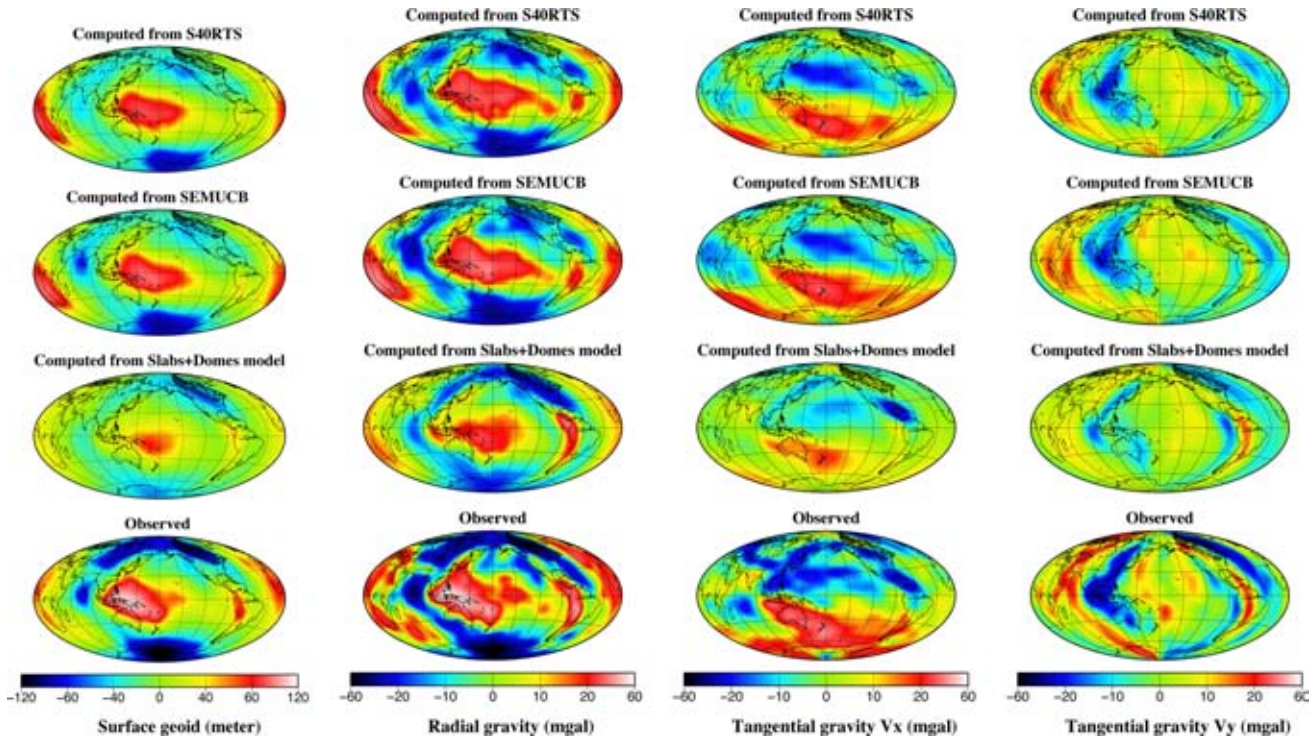


**Figure 10.** Surface geoid (column 1), gravity at the altitude of the GOCE satellite  $V_Z$  (column 2),  $V_X$  (column 3) and  $V_Y$  (column 4). For each data type, the computed data for the two tomographic models (S40RTS and SEMUCB) and for the geodynamic model as well as the observed data are plotted up to degree 20.

section a geodynamic model for the large-scale pattern of mantle dynamics with contributions due to subducted lithosphere and to long-wavelength convective instabilities.

## 5 JOINT ANALYSIS BASED ON A GEODYNAMIC MODEL

We use a simple geodynamic model for the large-scale pattern of mantle dynamics, in which we combine contributions due to subducted lithosphere and long-wavelength upwellings (Rouby *et al.* 2010). We use the model of mantle density heterogeneity derived by Ricard *et al.* (1993), based on plate-motion reconstructions under the assumption that subducted slabs have been sinking vertically into the mantle since 120 Ma. Plates are supposed to subduct down to the core–mantle boundary; the model assumes that their thickness increases by a factor 4 in the lower mantle. This factor as well as the sinking speed are dependent on the viscosity ratio between lower and upper mantle. The slabs are modeled as large sheets of cold material sinking down to the lower mantle with a density contrast  $\Delta\rho$  with respect to the PREM average densities throughout the mantle. This density contrast can vary as a function of depth since slabs pond in the transition zone and atop 1000 km.

The distribution of mass anomalies associated with deep structures such as thermochemical domes is based on an analysis of deep mantle seismic tomography, assuming a constant density contrast  $\Delta\rho^D$ .

In the initial geodynamic model,  $\Delta\rho$  was set to  $80 \text{ kg m}^{-3}$  (Ricard *et al.* 1993) and  $\Delta\rho^D = -50 \text{ kg m}^{-3}$  (Rouby *et al.* 2010). So we put here  $\Delta\rho^D = -\frac{5}{8}\Delta\rho$ .

We perform a Monte Carlo search for the viscosity  $\nu_2, \nu_3, \nu_4$  and for the density contrast of the slabs and of the domes with respect

to the surrounding mantle  $\Delta\rho_2, \Delta\rho_3$  and  $\Delta\rho_4$  of the three layers. We are aware that it is somewhat inconsistent to use a given density model and then vary the viscosity structure, whereas different viscosity structure would imply different sinking speed and hence different density structure. But the geometry of our ‘Slabs+Domes’ model is well correlated with the tomographic model for large wavelengths, and the results presented here will be discussed in term of the sensitivity of the gravity gradients.

We use the geometry of our ‘Slabs+Domes’ model and try to infer, from the gravity data, the viscosity profile and the depth variable density contrast between the subducted plates and the surrounding mantle. Because most of the masses are in the lower mantle in this geodynamic mantle density heterogeneities model, and in order to save computation time, we use our three-layer mantle instead of the four-layer model: upper mantle (100–670 km), upper part of the lower mantle (670–1150 km) and lower mantle (1150 km–CMB).

We compute 10 variance reductions which are now functions of six parameters, and similarly to the previous sections, for each pair of parameters, we compute the maximum variance reduction obtained for all the other parameters (Appendix B, Figs B7 and B8).

The values obtained for the maximum probability (eq. 18) are given in Table 5 and the viscosity profile is plotted in Fig. 9 (cyan line). The  $N$  variance reductions associated with this best model are given in the sixth column of the Table 6.

We compute the marginal probability and find that the density contrast  $\Delta\rho_2$  in the upper mantle and the viscosity in the top of the lower mantle  $\nu_3$  are not well estimated, with associated marginal probabilities about 0.05. An explanation for the density contrast  $\Delta\rho_2$  may be that, in the upper mantle, the diving slabs are narrow—100 km thick—sheets; consequently, they are not seen by our large-wavelength gravity signal expanded in spherical harmonics up to degree 20 ( $\simeq 2000 \text{ km}$ ).

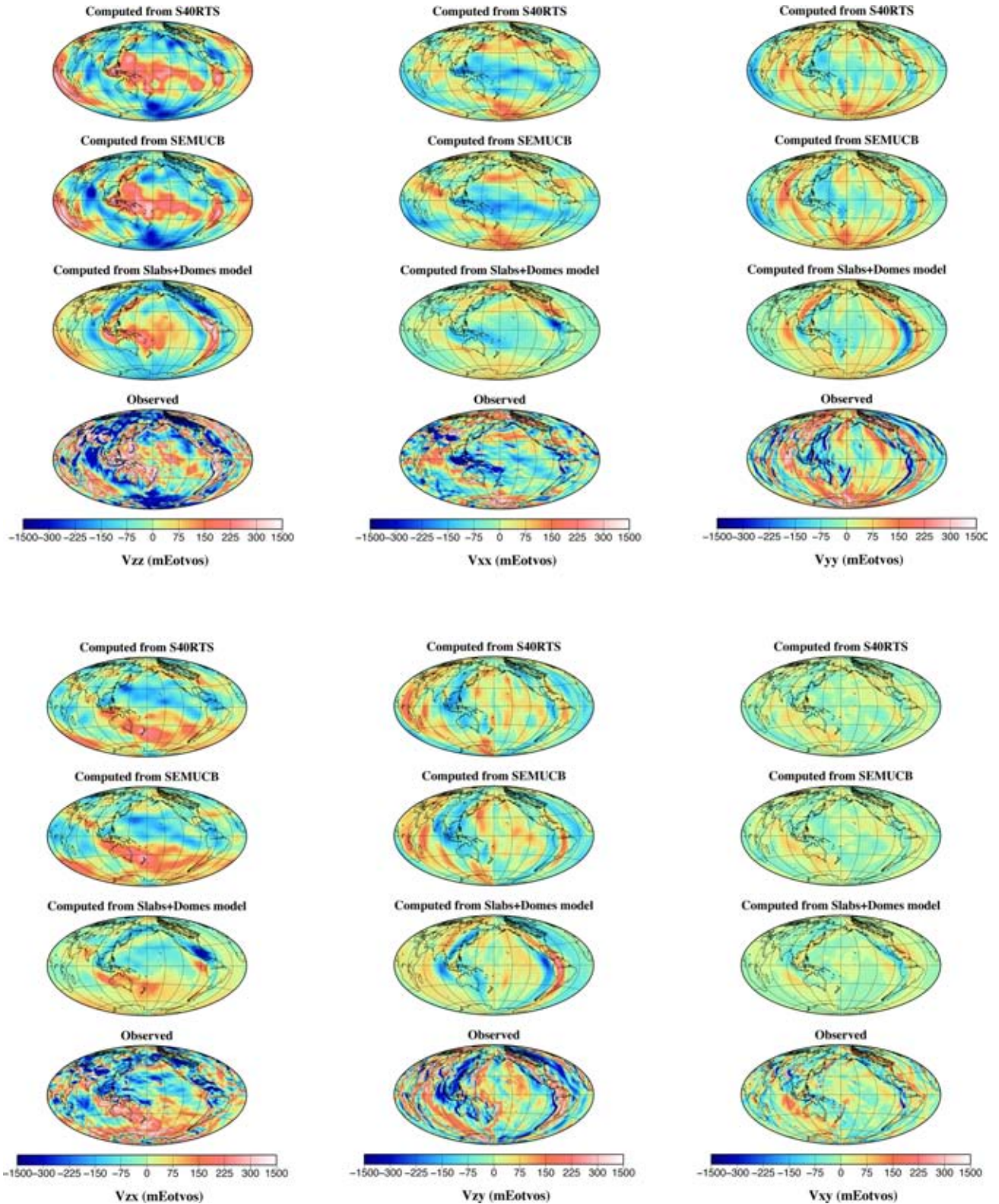


**Figure 11.** Gravity gradients at the altitude of the GOCE satellite: for each data type, the computed model for the two tomographic models (S40RTS and SEMUCB) and for the geodynamic model up to degree 20 are plotted as well as the observed data on the global grids with a constant step size of  $0.2^\circ$ .

The expected values and standard deviations obtained for the density contrast and for the  $\log_{10}$  of the viscosities are given in Table 5. Note that the viscosities are very similar to the ones obtained from the  $S$ -wave S40RTS tomographic data, for the three-layer mantle.

The viscosities of the upper and lower mantles are also similar to the ones obtained by Ricard *et al.* (1993) with a viscosity ratio  $\frac{\nu_1}{\nu_2}$  of about 40. In the layer 670–1150 km, the density contrast between the slabs and the surrounding mantle is about  $9 \text{ kg m}^{-3}$ ,

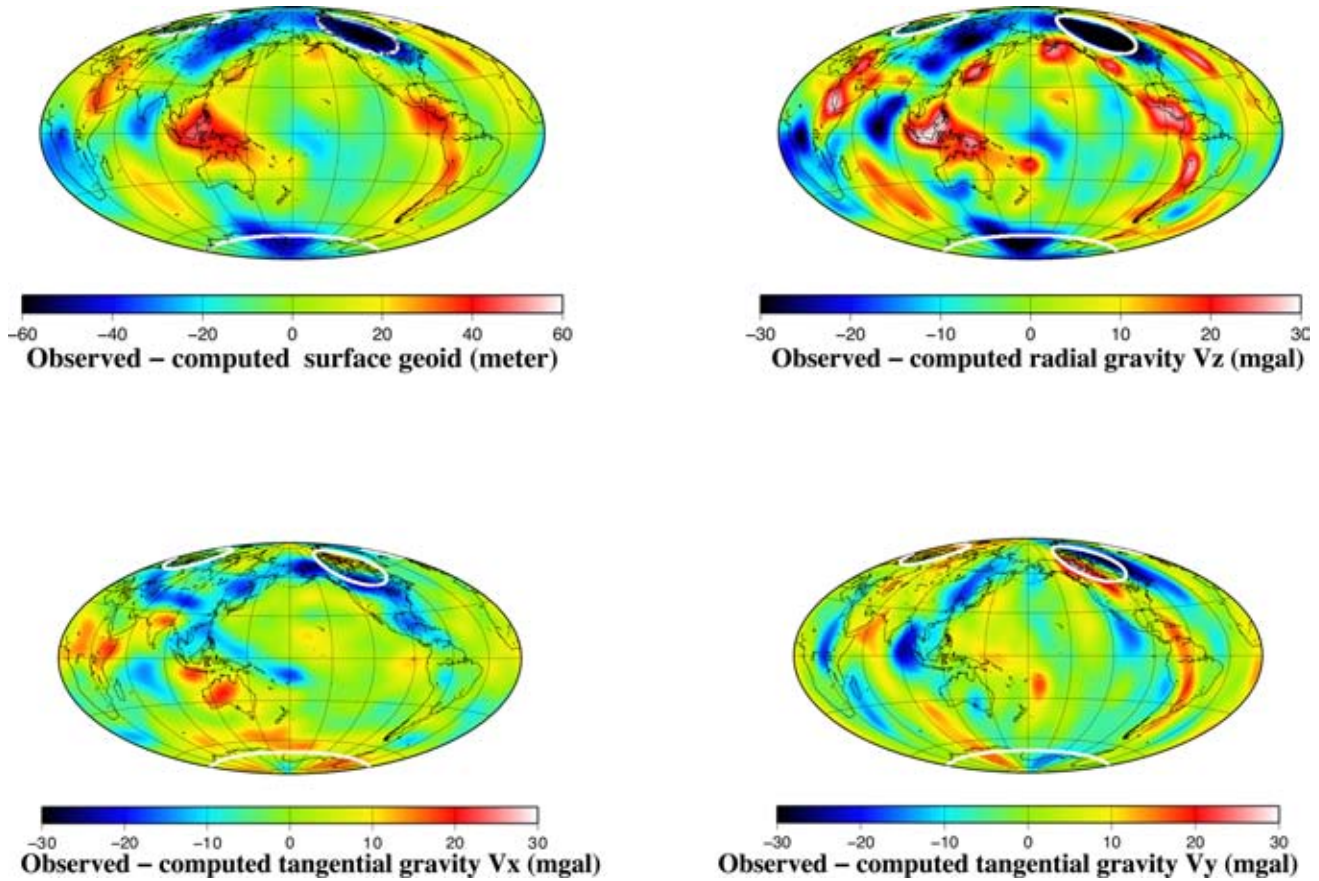


**Figure 12.** Discrepancy between the observation and the model obtained for S40RTS tomographic model, for the geoid at the surface (left-top), the gravity at the altitude of the GOCE satellite  $V_z$  (right-top),  $V_x$  (left-bottom) and  $V_y$  (right-bottom). The white small circle indicate the location of the ancient ice sheets, regions where Glacial Isostatic Adjustment is important.

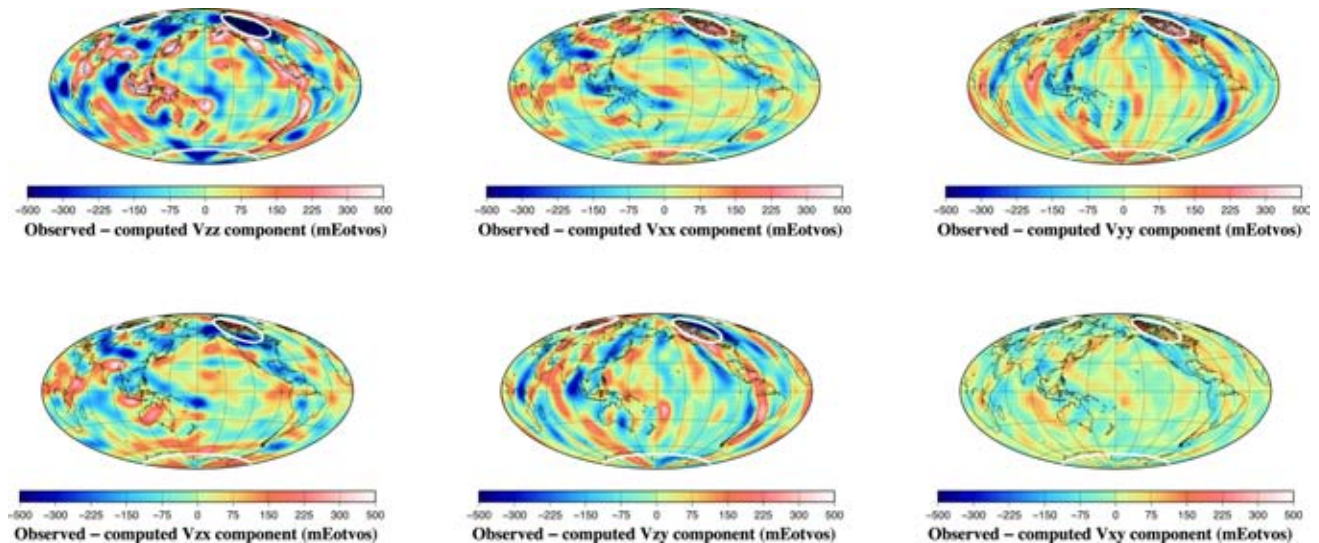


**Figure 13.** Discrepancy between the observation and the model obtained for S40RTS tomographic model, for the six components of the gravity gradient at the altitude of the GOCE satellite.

a value smaller than the  $80 \text{ kg m}^{-3}$  set by Ricard *et al.* (1993), suggesting that there are too many slabs in this part of the lower mantle in our model. In the lower mantle, we obtain a density contrast about  $52 \text{ kg m}^{-3}$  for the slabs and  $-32.5 \text{ kg m}^{-3}$  for the domes—note that these values are based on a radially averaged estimation.

We compute and plot the geoid, and the three components of gravity associated with the best model described above, in Fig. 10, from degree 2 up to 20, as well as the six components of the gravity gradient at the GOCE satellite altitude (Fig. 11).

The north–south elongated  $V_{YY}$  anomalies in our model over Asia and America follow the belt of geoid lows that surrounds the

**Table 5.** Density contrast of the slabs with respect to the lower mantle (in  $\text{kg m}^{-3}$ ) and  $\log_{10}$  (viscosity in Pa s) values for our geodynamic mantle density heterogeneities model: expected value and standard deviation computed from (20), best model obtained from the maximum probability (eq. 18).

|              | Density ( $\text{kg m}^{-3}$ )                |            | $\log_{10}$ (Viscosity in Pa s)               |            |
|--------------|---|------------|---|------------|
|              | Expected value<br>$\pm$<br>standard deviation | Best model | Expected value<br>$\pm$<br>standard deviation | Best model |
| Upper mantle | $56 \pm 34$                                   | 44         | $20.23 \pm 0.51$                              | 20.96      |
| 670–1150 km  | $22 \pm 16$                                   | 9          | $22.92 \pm 0.55$                              | 23.69      |
| 1150–2890 km | $35 \pm 25$                                   | 52         | $21.96 \pm 0.47$                              | 22.57      |

**Table 6.** Variance reductions for the best models given, respectively, in Tables 1–5.

| Mantle Tomographic model | Two-layer S40RTS | Three-layer S40RTS | Four-layer S40RTS | Four-layer SEMUCB | Three-layer ‘Slabs+Domes’ |
|--------------------------|------------------|--------------------|-------------------|-------------------|---------------------------|
| $\Phi^{\text{Geoid}}$    | 0.648            | 0.723              | 0.806             | 0.796             | 0.706                     |
| $\Phi^{V_z}$             | 0.535            | 0.590              | 0.649             | 0.661             | 0.607                     |
| $\Phi^{V_x}$             | 0.568            | 0.634              | 0.678             | 0.663             | 0.644                     |
| $\Phi^{V_y}$             | 0.425            | 0.454              | 0.522             | 0.582             | 0.500                     |
| $\Phi^{V_{zz}}$          | 0.311            | 0.336              | 0.364             | 0.398             | 0.376                     |
| $\Phi^{V_{xx}}$          | 0.324            | 0.345              | 0.349             | 0.334             | 0.357                     |
| $\Phi^{V_{yy}}$          | 0.267            | 0.293              | 0.336             | 0.410             | 0.357                     |
| $\Phi^{V_{zx}}$          | 0.326            | 0.356              | 0.368             | 0.370             | 0.378                     |
| $\Phi^{V_{zy}}$          | 0.236            | 0.249              | 0.286             | 0.357             | 0.310                     |
| $\Phi^{V_{xy}}$          | 0.183            | 0.193              | 0.212             | 0.266             | 0.236                     |

Pacific Ocean, recording Mesozoic slabs remnants in the lower mantle, with an enhanced geometric and depth information as compared to geoid data. The  $V_{zz}$  maxima in the Pacific Ocean and South of the African continent coincide with the locations of the LLSVP at the bottom of the lower mantle and the geoid highs but with a too small amplitude. The  $V_{xx}$ -gradient directionality underlines elongated east–west negative anomalies, following the former Tethyan subduction system and along the present-day Indonesia subduction.

These results extend the previous analysis of Panet *et al.* (2014) to a wider range of models.

## 6 CONCLUSIONS

In this paper, we have performed a joint analysis of the gradiometric data with seismological and geodynamic observations to estimate the viscosity and the mass anomalies within the mantle.

We have first used lateral variations in the Earth’s mantle deduced from two seismic tomography models and we have estimated the radial profiles for the density/velocity scaling factor and the viscosity which provide the best fit to the surface geoid, the gravity and the gravity gradients at the GOCE satellite altitude. We have found that the gradient of gravity improves the estimate of the scaling factor within the upper mantle, whereas the geoid and the gravity better constrain the lower mantle. In the upper mantle, the scaling factor is less than 0.02 for the upper part and about 0.08–0.14 for the lower part. Significantly larger values are found for depth greater than 1200 km (about 0.32–0.34).

In all cases, the scaling factor in the top of the lower mantle (between 670 and 1150 km depth) is not well estimated. To assess whether this lack of resolution would be related to a lack of signal in tomography models at these depths, mantle lateral variations associated with cold slabs sinking vertically into the mantle have then been used to estimate the density contrast between the slab

and the surrounding mantle as well as the mantle viscosity profiles. Our results have shown that there is too much slabs mass in the 670–1150 km layer in our model.

The viscosity profile obtained for these different mantle density heterogeneities are similar and characterized by a decrease in the lower part of the upper mantle (about  $10^{20}$ – $2 \times 10^{20}$  Pa s) and by an increase (about  $10^{23}$ – $2 \times 10^{23}$  Pa s) at the top of the lower mantle (between 670 and 1150 km). The viscosity of the mantle below 1150 km depth is well estimated, with values about  $10^{22}$ – $4 \times 10^{22}$  Pa s.

A recent study (Rudolph *et al.* 2015) based on a reanalysis of the long-wavelength non-hydrostatic geoid and having no a-priori assumption about the layering of the mantle has obtained a decrease of the viscosity between 670 and ~800 km, following by an increase in a layer between ~800 and 1000 km. This study has assumed a fixed scaling factor (from Stixrude & Lithgow-Bertelloni 2007) ranging from 0.3 up to 0.5, that is to say similar to the one we have estimated from the geoid alone and greatly larger than the one we have estimated from our maximum probability. In our analysis, we have chosen to estimate simultaneously the scaling factor and the viscosity. So, because the number of reliably estimated parameters cannot considerably increase, we have set the locations of the layers. It is consequently difficult to compare our results with theirs. We have done a simple last test: we have changed the depth of the different layers between 670 and 1150 km (670–800 km and 800–1150 km) and we have reiterated our analysis to investigate the contribution of the gravimetric gradients to infer mantle properties in this region. We have obtained a similar decrease of the viscosity between 670 and 800 km following by an increase in the layer 800–1150 km. Nevertheless we have found that these parameters are not well estimated, with a marginal probability slightly above the uniform distribution.

Finally, a future study could be a similar joint analysis of GOCE gravity gradients with seismological observations to infer a scaling factor in the lower mantle with lateral variations, at least in

the LLSVPs, to reduce the discrepancy between the observed and calculated data in these regions.

Shallow sources such as the static contribution of the GIA, plumes in the upper-mantle or oceanic ridges will be interpreted at regional scales from the residual geoid, gravity and gravity gradients.

## ACKNOWLEDGEMENTS

We thank S. French for giving us the coefficients of the spherical harmonic expansion of the seismic velocity model SEMUCB. We also gratefully acknowledge B. Romanowicz for her helpful comments on the original manuscript and F. Chambat and B. Steinberger for their constructive reviews. This study was supported by CNES (Centre National d'Etudes Spatiales) through the TOSCA committee and is IGP contribution number 3701.

## REFERENCES

- Bouman, J., Ebbing, J. & Fuchs, M., 2013. Reference frame transformation of satellite gravity gradients and topographic mass reduction, *J. geophys. Res.*, **118**, 759–774.
- Bouman, J. *et al.*, 2015. GOCE gravity gradient data for lithospheric modeling, *Int. J. Appl. Earth Obs. Geoinform.*, doi:10.1016/j.jag.2013.11.001.
- Cammarano, F., Goes, S., Vacher, P. & Giardini, D., 2003. Inferring upper-mantle temperatures from seismic velocities, *Phys. Earth planet. Inter.*, **138**, 197–222.
- Cammarano, F., Deuss, A., Goes, S. & Giardini, D., 2005. One-dimensional physical reference models for the upper mantle and transition zone: combining seismic and mineral physics constraints, *J. geophys. Res.*, **110**, B01306, doi:10.1029/2004JB003272.
- Casotto, S. & Fantino, E., 2009. Gravitational gradients by tensor analysis with application to spherical coordinates, *J. Geod.*, **83**, 621–634.
- Chambat, F., Ricard, Y. & Valette, B., 2010. Flattening of the Earth: further from hydrostaticity than previously estimated, *Geophys. J. Int.*, **183**, 727–732.
- Dziewonski, A.M. & Anderson, D.L., 1981. Preliminary reference Earth model PREM, *Phys. Earth planet. Inter.*, **25**, 297–356.
- Ebbing, J., Bouman, J., Fuchs, M., Gradmann, S. & Haagmans, R., 2014. Sensitivity of GOCE gravity gradients to crustal thickness and density variations—case study for the Northeast Atlantic Region, in *LAG Symposia Series*, Vol. 141, doi:10.1007/978-3-319-10837-7\_37.
- Flechtner, F., Dahle, C., Neumayer, K.H., König, R. & Förste, C., 2010. The Release 04 CHAMP and GRACE EIGEN gravity field models, in *System Earth via Geodetic-Geophysical Space Techniques*, pp. 41–58, eds Flechtner, F., Gruber, T., Güntner, A., Manda, M., Rothacher, M., Schöne, T. & Wickert, J., Springer.
- Förste, C. *et al.*, 2008. The GeoForschungsZentrum Potsdam/Groupe de Recherche de Géodésie Spatiale satellite-only and combined gravity field models: EIGEN-GL04S1 and EIGEN-GL04C, *J. Geod.*, **82**(6), 331–346.
- Forte, A.M., 2007. Constraints on seismic models from other disciplines—implications for mantle dynamics and composition, in *Treatise of Geophysics*, Vol. 1, pp. 805–857, Elsevier.
- Forte, A.M. & Perry, H.K.C., 2000. Geodynamic evidence for a chemically depleted continental tectosphere, *Science*, **290**, 1940–1944.
- Forte, A.M., Woodward, R.L. & Dziewonski, A.M., 1994. Joint inversions of seismic and geodynamic data for models of three-dimensional mantle heterogeneity, *J. geophys. Res.*, **99**, 21 857–21 877.
- Forte, A.M., Mitrovica, J.X. & Espeset, A., 2002. Geodynamic and seismic constraints on the thermochemical structure and dynamics of convection in the deep mantle, *Phil. Trans. R. Soc. Lond., A.*, **360**, 2521–2543.
- French, S.W. & Romanowicz, B.A., 2014. Whole-mantle radially anisotropic shear velocity structure from spectral-element waveform tomography, *Geophys. J. Int.*, **199**, 1303–1327.
- Greff-Lefftz, M., Métivier, L. & Besse, J., 2010. Dynamic mantle density heterogeneities and global geodetic observables, *Geophys. J. Int.*, **180**(3), 1080–1094.
- Hager, B.H., 1984. Subducted slabs and the geoid: constraints on mantle rheology and flow, *J. geophys. Res.*, **89**(B7), 6003–6015.
- Kaban, M.K. & Trubitsyn, V., 2012. Density structure of the mantle transition zone and the dynamic geoid, *J. Geodyn.*, **59–60**, 183–192.
- Karato, S.-I. & Karki, B.B., 2001. Origin of lateral variation of seismic wave velocities and density in the deep mantle, *J. geophys. Res.*, **106**(B10), 21 771–21 783.
- Kaufmann, G. & Lambeck, K., 2000. Mantle dynamics, postglacial rebound and the radial viscosity profile, *Phys. Earth planet. Inter.*, **121**, 301–324.
- Koop, R., 1993. Global gravity field modelling using satellite gravity gradiometry, *PhD thesis*, Netherlands Geodetic Commission, Geodesy, series number 38.
- Lee, C.-K., Han, S.-C. & Steinberger, B., 2011. Influence of variable uncertainties in seismic tomography models on constraining mantle viscosity from geoid observations, *Phys. Earth planet. Inter.*, **184**, 51–62.
- Marquart, G., Steinberger, B. & Niehuus, K., 2005. On the effect of a low viscosity asthenosphere on the temporal change of the geoid—a challenge for future gravity missions, *J. Geodyn.*, **39**, 493–511.
- Métivier, L. & Greff-Lefftz, M., 2012. The static contribution of Glacial Isostatic Adjustment on the Geoid, in *2012 EGU General Conference Abstracts*, Vol. 14, EGU2012, p. 7563.
- Métivier, L., Caron, L., Greff-Lefftz, M., Pajot-Métivier, G., Fleitout, L. & Rouby, H., 2015. Evidence for postglacial signature in gravity gradients: a clue on lower mantle viscosity, *Earth planet. Sci. Lett.*, submitted.
- Mitrovica, J.X., 1996. Haskell (1935) revisited, *J. geophys. Res.*, **101**, 555–569.
- Moucha, R., Forte, A.M., Mitrovica, J.X. & Daradich, A., 2007. Lateral variations in mantle rheology: implications for convection related surface observables and inferred viscosity models, *Geophys. J. Int.*, **169**, 113–135.
- Nakiboglu, S.M., 1979. Hydrostatic figure and related properties of the Earth, *Geophys. J. R. astr. Soc.*, **57**, 639–648.
- Nakiboglu, S.M., 1982. Hydrostatic theory of the Earth and its mechanical implications, *Phys. Earth planet. Inter.*, **28**, 302–311.
- Panet, I., Pajot-Métivier, G., Greff-Lefftz, M., Métivier, L., Diament, M. & Manda, M., 2014. Mapping the mass distribution of Earth's mantle using satellite-derived gravity gradients, *Nature Geosci.*, **7**, 131–135.
- Ricard, Y., Vigny, C. & Froidevaux, C., 1989. Mantle heterogeneities, geoid, and plane motion—a Monte Carlo inversion, *J. geophys. Res.*, **94**, 13 739–13 754.
- Ricard, Y., Richards, M.A., Lithgow-Bertelloni, C. & Le Stunff, Y., 1993. A geodynamic model of mantle density heterogeneity, *J. geophys. Res.*, **98**, 21 895–21 909.
- Ricard, Y., Chambat, F. & Lithgow-Bertelloni, C., 2006. Gravity observations and 3D structure of the Earth, *C. R. Geosci. Intern. Geophys. (Phys. Earth's Inter.)*, **338**, 992–1001.
- Richards, M.A. & Hager, B.H., 1984. Geoid anomalies in a dynamic Earth, *J. geophys. Res.*, **89**, 5987–6002.
- Richards, M.A. & Engebretson, D.C., 1992. Large scale mantle convection and the history of subduction, *Nature*, **355**, 437–440.
- Ritsema, J., Deuss, A., van Heijst, H.J. & Woodhouse, J.H., 2011. S40RTS: a degree-40 shear-velocity model for the mantle from new Rayleigh wave dispersion, teleseismic traveltime and normal-mode splitting function measurements, *J. geophys. Res.*, **116**, 1223–1236.
- Rouby, H., Greff-Lefftz, M. & Besse, J., 2010. Mantle dynamics, geoid, inertia and TPW since 120 My, *Earth planet. Sci. Lett.*, **292**, 301–311.
- Rudolph, M., Lekic, V. & Lithgow-Bertelloni, C., 2015. Viscosity jump in Earth's mid-mantle, *Science*, **350**(6266), 1349–1352.
- Simmons, N.A., Forte, A.M. & Grand, S.P., 2009. Joint seismic, geodynamic and mineral physical constraints on three-dimensional mantle heterogeneity: implications for the relative importance of thermal versus compositional heterogeneity, *J. Geophys. Res.*, **114**, 1284–1304.
- Soldati, G., Boschi, L., Descamps, F. & Giardini, D., 2009. Inferring radial models of mantle viscosity from gravity (GRACE) data and an evolutionary algorithm, *Phys. Earth planet. Inter.*, **176**, 19–32.

Steinberger, B. & Calderwood, A.R., 2006. Models of large-scale viscous flow in the Earth's mantle with constraints from mineral physics and surface observations, *Geophys. J. Int.*, **167**, 1461–1481.

Stixrude, L., 2007. Properties of rocks and minerals—seismic properties of rocks and minerals, and structure of the Earth, in *Treatise on Geophysics*, Vol. 2, pp. 7–32, Elsevier.

Stixrude, L. & Lithgow-Bertelloni, C., 2007. Influence of phase transformations on lateral heterogeneity and dynamics in Earth's mantle, *Earth planet. Sci. Lett.*, **263**, 45–55.

Tkalcic, H. & Romanowicz, B., 2002. Short scale heterogeneity in the lowermost mantle: insights from PcP-P and ScS-S data, *Earth planet. Sci. Lett.*, **201**(1), 57–68.

## APPENDIX A: MEAN VALUES AND COVARIANCE MATRIX

We note  $X_i(r, \theta, \varphi)$  the data  $i$ , where  $r$  stands for  $r_E$  or  $r_h$  following the data. We compute the mean value of the data  $i$ ,  $\bar{X}_i$ :

$$\bar{X}_i = \frac{1}{S_E} \int_0^{2\pi} \int_{-\pi/2}^{\pi/2} X_i(r, \Psi, \varphi) dS$$

Note that on our hydrostatic reference ellipsoid, the mean values of  $V_X$ ,  $V_{XX}$ ,  $V_{YY}$  and  $V_{ZX}$  are not equal to zero. These are terms related to derivative with respect to the colatitude.

The covariance matrix  $C^D$  is computed from:

$$C_{ij} = \overline{X_i X_j} - \bar{X}_i \bar{X}_j \quad \text{with} \quad \overline{X_i X_j} = \frac{1}{S_E} \int_0^{2\pi} \int_{-\pi/2}^{\pi/2} X_i(r, \Psi, \varphi) X_j(r, \Psi, \varphi) dS$$

The standard deviation for the data  $i$  is simply  $\sigma_{X_i} = \sqrt{\overline{X_i X_i} - \bar{X}_i \bar{X}_i}$

And the covariance matrix is:

|          |          |          |          |          |          |          |          |          |          |
|----------|----------|----------|----------|----------|----------|----------|----------|----------|----------|
| 1721.62  | 804.539  | -54.6287 | 0.247410 | 6251.75  | -3015.42 | -3236.33 | -452.026 | -8.05868 | -314.002 |
| 804.539  | 406.384  | -21.9682 | 0.827751 | 3588.72  | -1730.28 | -1858.44 | -181.159 | 1.24925  | -216.885 |
| -54.6287 | -21.9682 | 176.136  | -24.4173 | -139.037 | -13.0891 | 152.126  | 1518.50  | -263.106 | -6.91264 |
| 0.247410 | 0.827751 | -24.4173 | 128.134  | 9.41114  | -1.24925 | -8.16189 | -262.886 | 1301.99  | -16.9193 |
| 6251.75  | 3588.72  | -139.037 | 9.41114  | 39151.5  | -19062.6 | -20088.9 | -1145.46 | 19.5071  | -2463.65 |
| -3015.42 | -1730.28 | -13.0891 | -1.24925 | -19062.6 | 11505.4  | 7557.27  | 102.836  | 1.51413  | 1163.65  |
| -3236.33 | -1858.44 | 152.126  | -8.16189 | -20088.9 | 7557.27  | 12531.6  | 1042.62  | -21.0212 | 1300.0   |
| -452.026 | -181.159 | 1518.50  | -262.886 | -1145.46 | 102.836  | 1042.62  | 23251.9  | -2983.85 | -19.6161 |
| -8.05868 | 1.24925  | -263.106 | 1301.99  | 19.5071  | 1.51413  | -21.0212 | -2983.85 | 15914.2  | -33.3791 |
| -314.002 | -216.885 | -6.91264 | -16.9193 | -2463.65 | 1163.65  | 1300.0   | -19.6161 | -33.3791 | 2517.35  |

**Table A1.**

| Data           | Geoid<br>(m) | $V_Z$<br>(mGal) | $V_X$<br>(mGal) | $V_Y$<br>(mGal) | $V_{ZZ}$<br>(mE) | $V_{XX}$<br>(mE) | $V_{YY}$<br>(mE) | $V_{ZX}$<br>(mE) | $V_{ZY}$<br>(mE) | $V_{XY}$<br>(mE) |
|----------------|--------------|-----------------|-----------------|-----------------|------------------|------------------|------------------|------------------|------------------|------------------|
| $i$            | 1            | 2               | 3               | 4               | 5                | 6                | 7                | 8                | 9                | 10               |
| $\bar{X}_i$    | 0            | 0               | 0.7             | 0               | 0                | -14              | 14               | 6                | 0                | 0                |
| $\sigma_{X_i}$ | 41           | 20              | 13              | 11              | 198              | 107              | 112              | 152              | 126              | 50               |

**APPENDIX B: VARIANCE REDUCTION**

**Variance reduction for the three-layered model**

Variance reduction for the surface geoid, for the gravity and the gravity gradients at the altitude  $h$  above the hydrostatic reference ellipsoid. There are 15 possible combinations of two out of six variables. We only plot here the nine combinations related to pairs of viscosity, pairs of scaling factor or pairs of viscosity and scaling factor in the same layer.

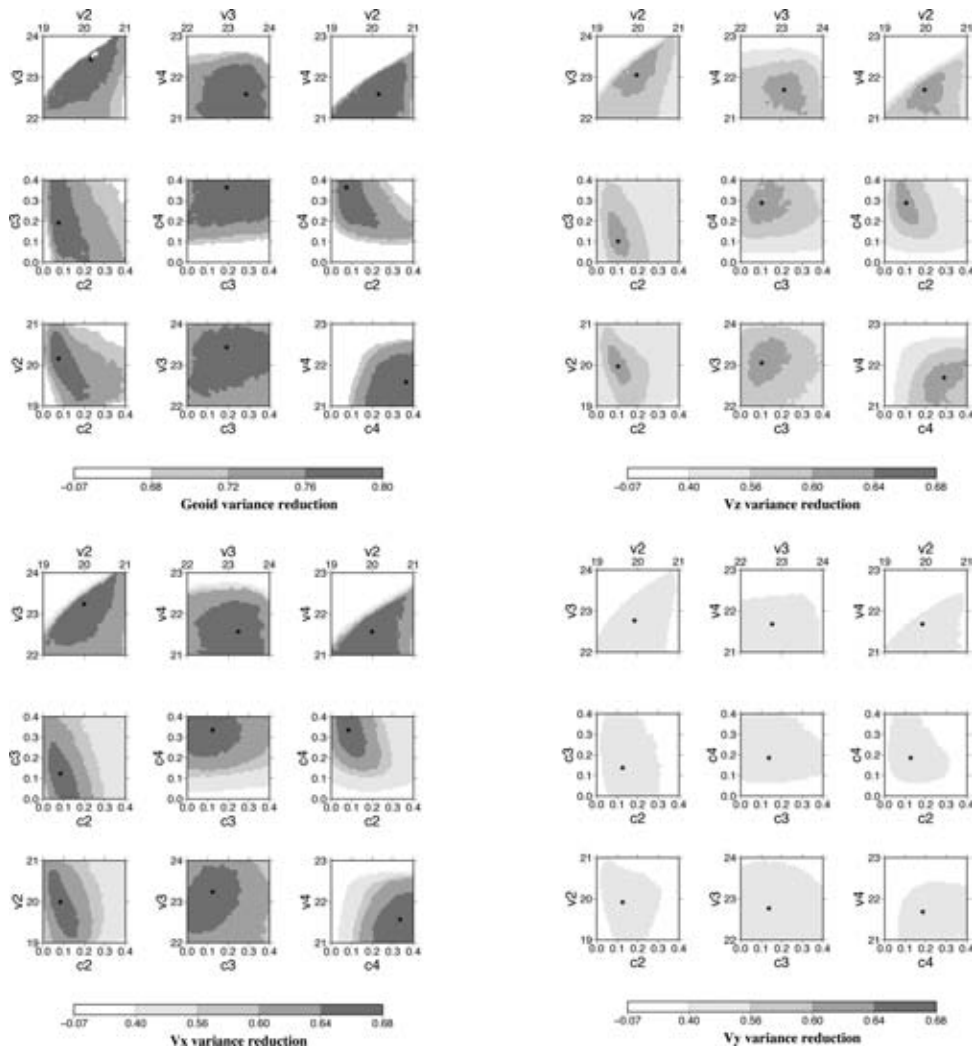


**Figure B1.** Variance reduction for the surface geoid and for the gravity at the altitude of the GOCE satellite. The black star corresponds to the best model for the data.

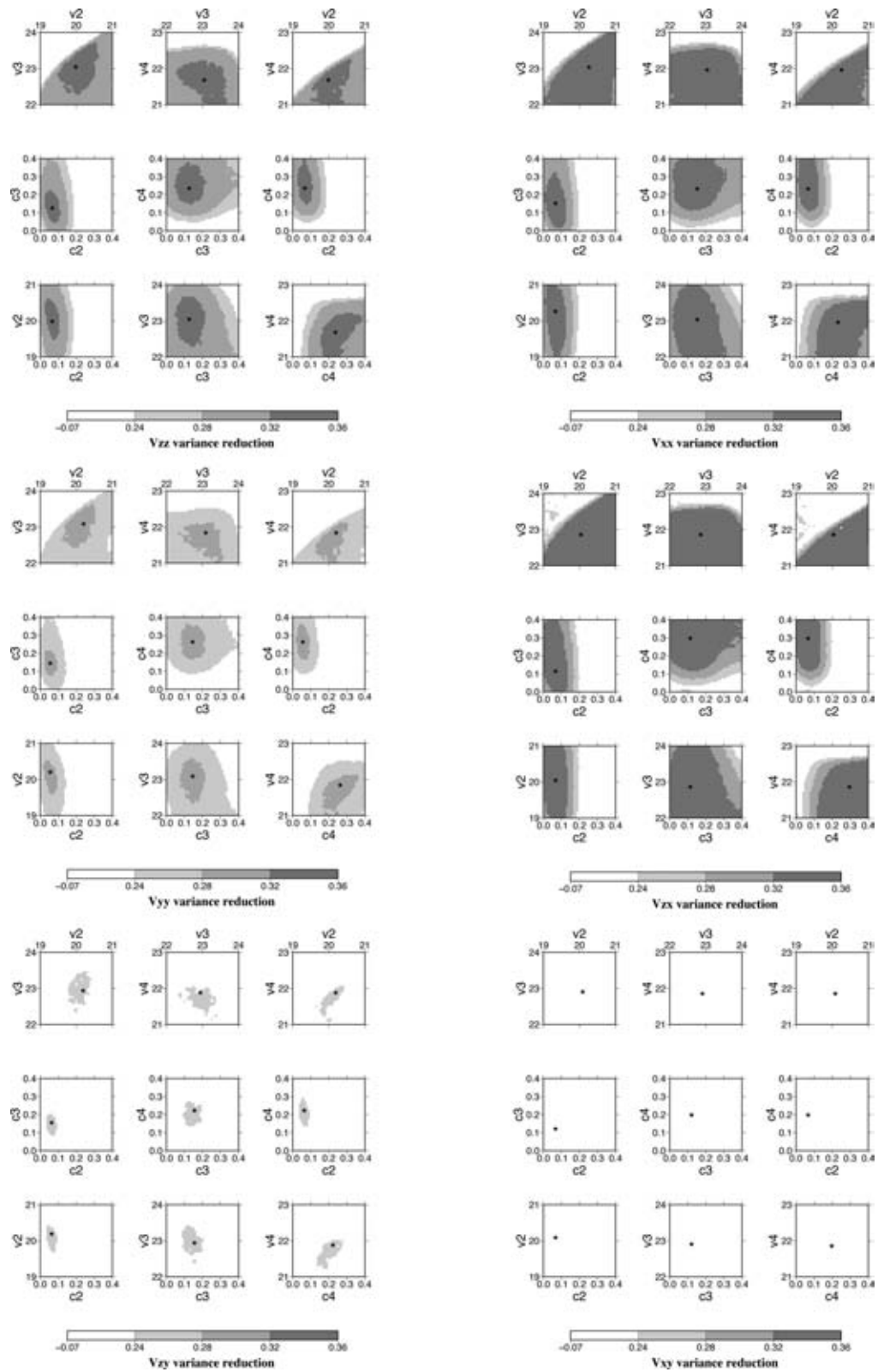


**Figure B2.** Variance reduction for the six components of the gravimetric gradients at the altitude of the GOCE satellite. The black star corresponds to the best model obtained for the data.

**Variance reduction for the four-layered model—S40RTS**

Variance reduction for the surface geoid, for the gravity and the gravity gradients at the altitude  $h$  above the hydrostatic reference ellipsoid. There are 28 possible combinations of two out of eight variables. We only plot here the 16 combinations related to pairs of viscosity, pairs of scaling factor or pairs of viscosity and scaling factor in the same layer.

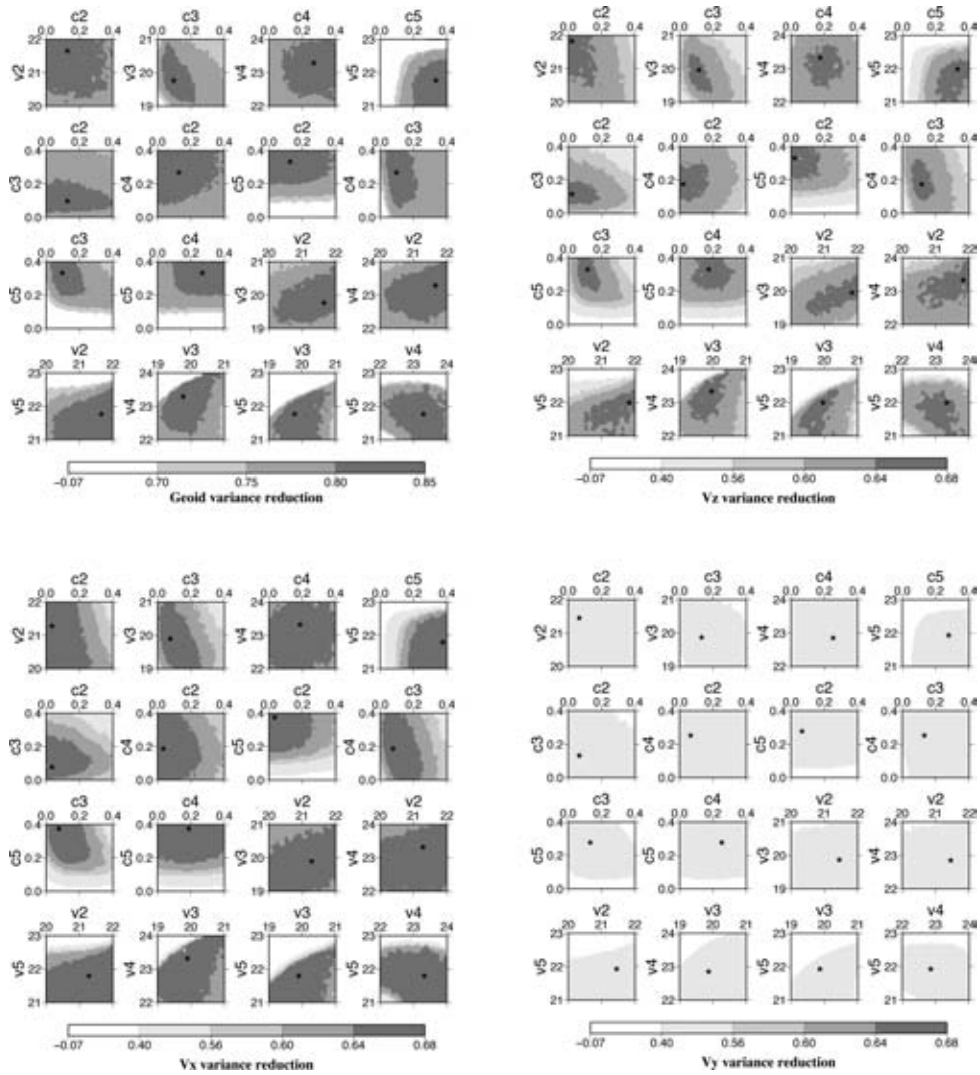


**Figure B3.** Same as Fig. B1.

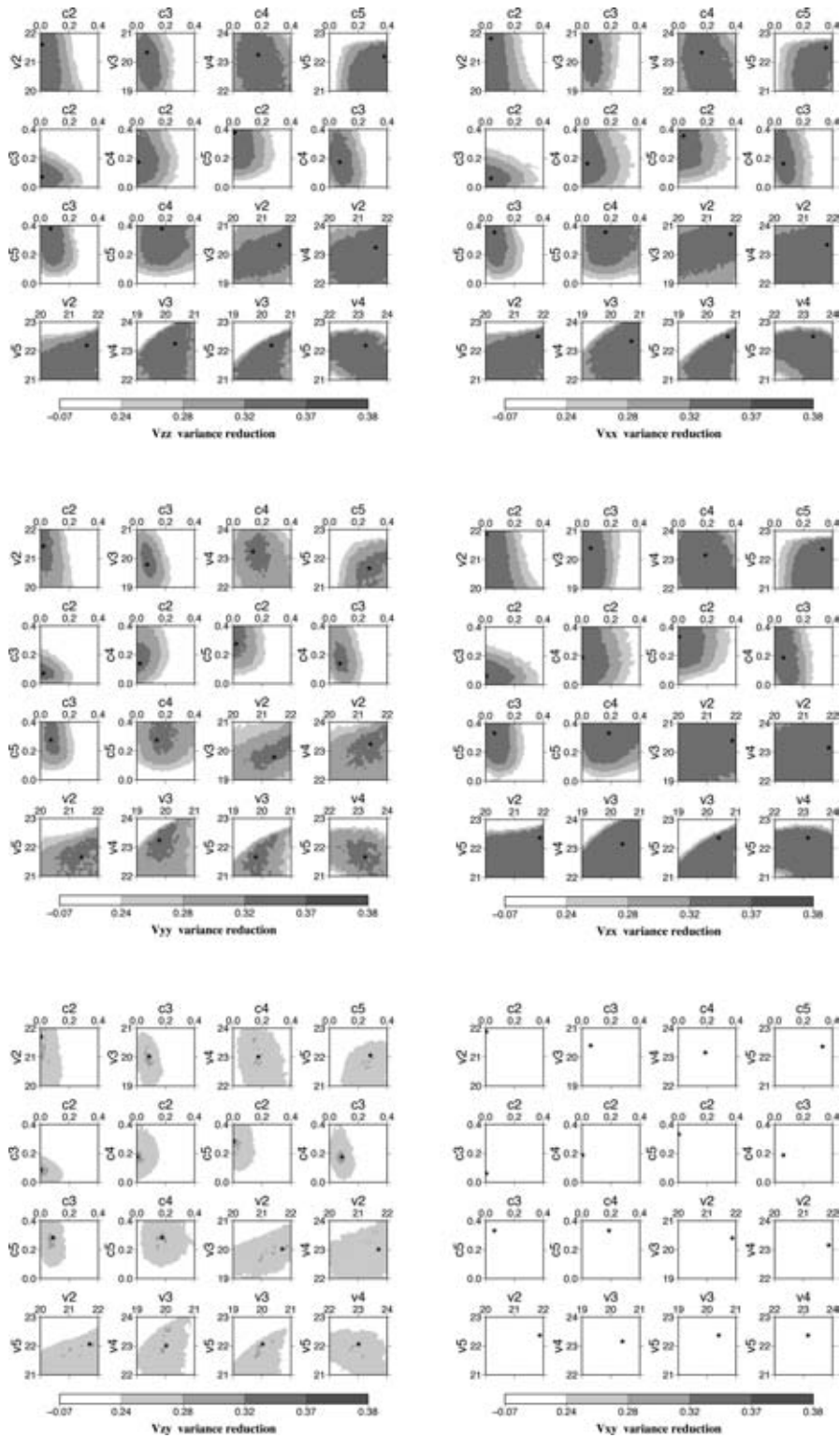


Figure B4. Same as Fig. B2.

**Variance reduction for the four-layered model—SEMUCB**

Variance reduction for the surface geoid, for the gravity and the gravity gradients at the altitude  $h$  above the hydrostatic reference ellipsoid.

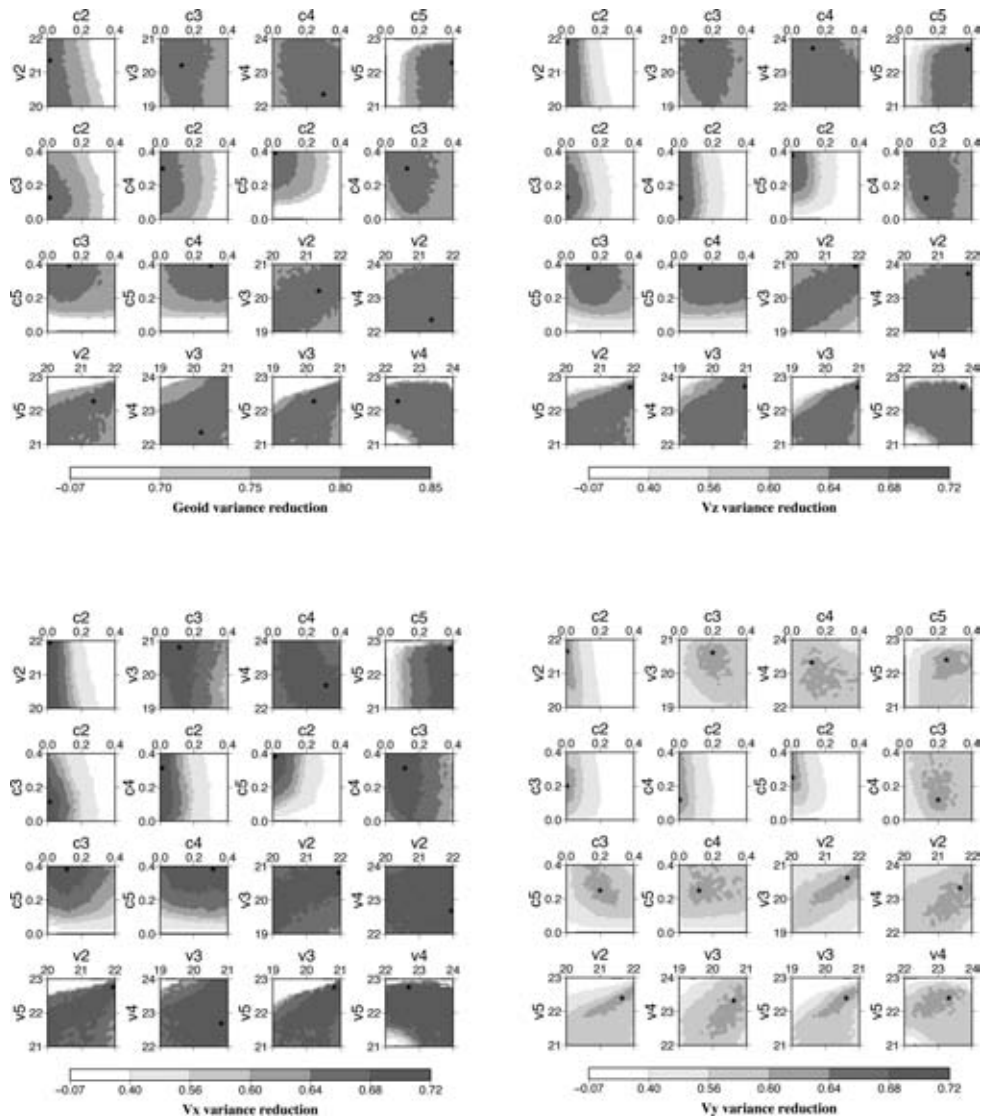


Figure B5. Same as Fig. B1.

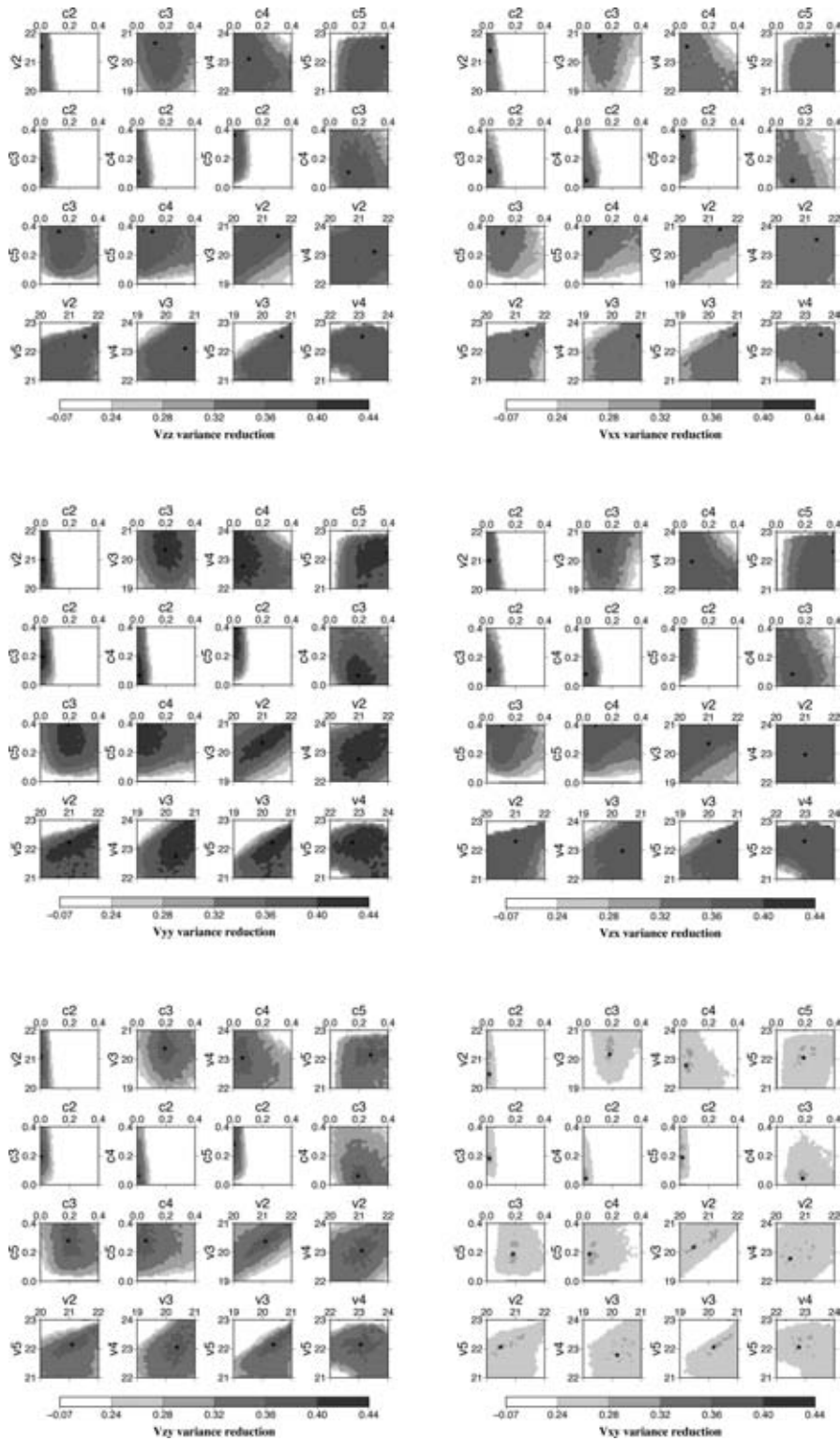
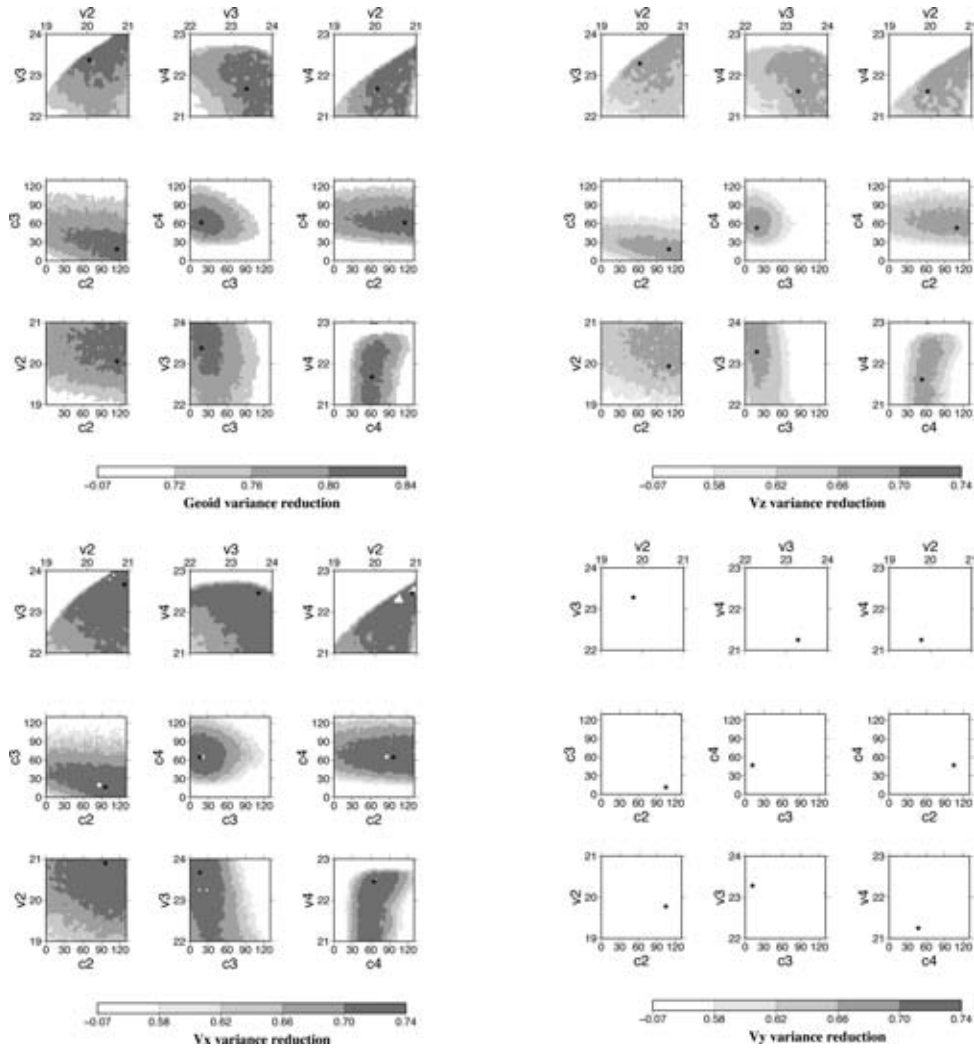


Figure B6. Same as Fig. B2.

**Variance reduction for the three-layered model—‘Slabs+Domes’**

Variance reduction for the surface geoid, for the gravity and the gravity gradients at the altitude  $h$  above the hydrostatic reference ellipsoid.



**Figure B7.** Same as Fig. B1.

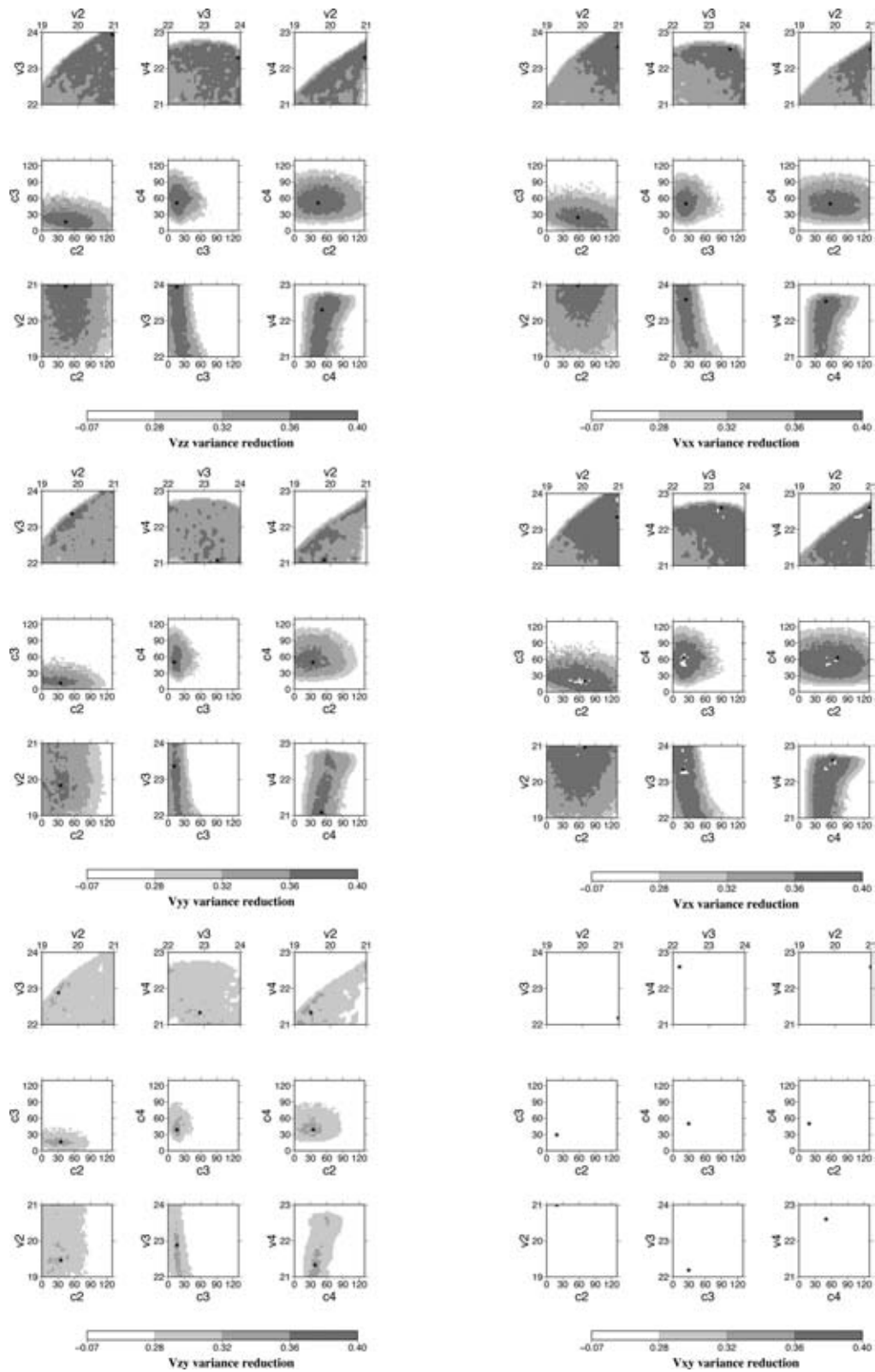


Figure B8. Same as Fig. B2.